In situ zircon U-Pb, Lu-Hf, $\delta^{18}O$, and trace elements from intrusive units in northern Hogem batholith, Quesnel terrane, north-central British Columbia

G. Jones, L. Ootes,
Y. Luo, R. Stern,
A. Vezinet, D.G. Pearson

Ministry of
Energy, Mines and
Low Carbon Innovation

GeoFile 2022-09

Ministry of Energy, Mines and Low Carbon Innovation
Mines, Competitiveness, and Authorizations Division
British Columbia Geological Survey

Recommendation citation: Jones, G., Ootes, L., Luo, Y., Stern, R., Vezinet, A., and Pearson, D.G., 2022. In situ zircon U-Pb, Lu-Hf, $\delta^{18}O$, and trace elements from intrusive units in northern Hogem batholith, Quesnel terrane, north-central British Columbia. British Columbia Ministry of Energy, Mines and Low Carbon Innovation, British Columbia. Geological Survey GeoFile 2022-09, 19p.

Front cover: On distant ridge, intrusive contact between the Osilinka suite granite (left, light toned) and Thane Creek suite diorite (right, dark toned). Contact dips steeply and extends in a valley from the middle skyline to the small lake, lower left. Hogem batholith, south-central British Columbia.

Back cover: Backscatter electron image of a subset of zircon separates from hornblendite sample 18lo22-1a, Thane Creek suite.

BRITISH
COLUMBIA

Ministry of
Energy, Mines and
Low Carbon Innovation

In situ zircon U-Pb, Lu-Hf, δ^{18}O, and trace elements from intrusive units in northern Hogem batholith, Quesnel terrane, north-central British Columbia

G. Jones
L. Ootes
Y. Luo
R. Stern
A. Vezinet
D.G. Pearson

Ministry of Energy, Mines and Low Carbon Innovation
British Columbia Geological Survey
GeoFile 2022-09

In situ zircon U-Pb, Lu-Hf, $\delta^{18}O$, and trace elements from intrusive units in northern Hogem batholith, Quesnel terrane, north-central British Columbia

G. Jones[1], L. Ootes[2a], Y. Luo[1], R. Stern[1], A. Vezinet[1], and D.G. Pearson[1]

[1]Department of Earth & Atmospheric Sciences, University of Alberta, Edmonton, AB, T6G 2E3
[2]British Columbia Geological Survey, Ministry of Energy, Mines and Low Carbon Innovation, Victoria, BC, V8W 9N3
[a]corresponding author: luke.ootes@gov.bc.ca

Recommendation citation: Jones, G., Ootes, L., Luo, Y., Stern, R., Vezinet, A., and Pearson, D.G., 2022. In situ zircon U-Pb, Lu-Hf, $\delta^{18}O$, and trace elements from intrusive units in northern Hogem batholith, Quesnel terrane, north-central British Columbia. British Columbia Ministry of Energy, Mines and Low Carbon Innovation, British Columbia. Geological Survey GeoFile 2022-09, 19 p.

Abstract
New and refined geochronology and geochemistry results complement bedrock mapping in northern Hogem batholith, Quesnel terrane. Data and interpretations presented here include 13 new and refined U-Pb zircon crystallization ages and five new U-Pb titanite crystallization ages, determined by LA-ICP-MS. These are supported by zircon oxygen-isotope data, determined by SIMS, and zircon Lu-Hf and trace elements. and titanite and apatite Sm-Nd results, determined by LA-ICP-MS.

Keywords: Hogem batholith, Quesnel terrane, geochronology; isotope geochemistry, U-Pb zircon crystallization ages, trace elements; Lu-Hf, Sm-Nd, oxygen isotopes, apatite, titanite, LA-ICP-MS, SIMS

1. Introduction

In 2018, the British Columbia Geological Survey initiated a three-year mapping project in the Omineca Mountains of north-central British Columbia to better understand the geology and associated base- and precious-metal mineralization in the northern part of Hogem batholith and adjacent supracrustal rocks of the Quesnel, Stikine, and Cache Creek terranes (Ootes et al., 2019, 2020a,b,c). Herein we present analytical results from samples collected during 2018 and 2019 mapping. These results include U-Pb, Lu-Hf, and trace element analyses of zircon and supplementary U-Pb and Sm-Nd analyses of titanite and apatite data using laser ablation inductively coupled plasma mass-spectrometry (LA-ICP-MS), and zircon oxygen-isotope data using secondary ion mass spectrometry (SIMS). Most of the U-Pb igneous zircon crystallization ages were previously reported by Ootes et al. (2020c) and Jones et al. (2021); some are refined herein. This GeoFile serves as a data repository for an M.Sc. thesis study on zircon geochemistry of the Hogem batholith (Jones, 2022) and for forthcoming reports.

Nine appendices are included (BCGS_GF2022-09.zip). Appendix 1 includes a table of bedrock units and their salient features and a table of samples, locations, and analytical work completed on each sample. Images of zircon grain mounts with beam-spot locations are included in Appendix 2. Appendix 3 contains new zircon oxygen isotope data determined from SIMS. Appendix 4 contains new zircon U-Pb crystallization results and supporting data, determined from LA-ICP-MS. Appendix 5 contains new zircon Lu-Hf data, determined from LA-ICP-MS. Appendix 6 contains new zircon trace element data, determined from LA-ICP-MS. Appendix 7 contains combined zircon U-Pb crystallization age and Lu-Hf results and supporting data, determined from laser ablation split stream (LASS)-ICP-MS. Appendix 8 contains new combined zircon Lu-Hf and trace elements (TE) results, determined from LASS-ICP-MS. Appendix 9 contains new combined apatite and titanite U-Pb age and Sm-Nd results and supporting data, determined from LASS-ICP-MS.

2. Geology

Hogem batholith is in the Quesnel terrane and comprises Triassic to Cretaceous intrusions that intruded volcanic and sedimentary rocks of the Nicola Group (Triassic), which bound the batholith to the north and east (Figs. 1, 2). To the west, the batholith and Nicola Group rocks are juxtaposed against Cache Creek and Stikine terranes along the Pinchi-Ingenika dextral strike-slip fault system (Figs. 1, 2).

Hogem batholith is subdivided into four petrologically distinct intrusive units. From oldest to youngest these are the Thane

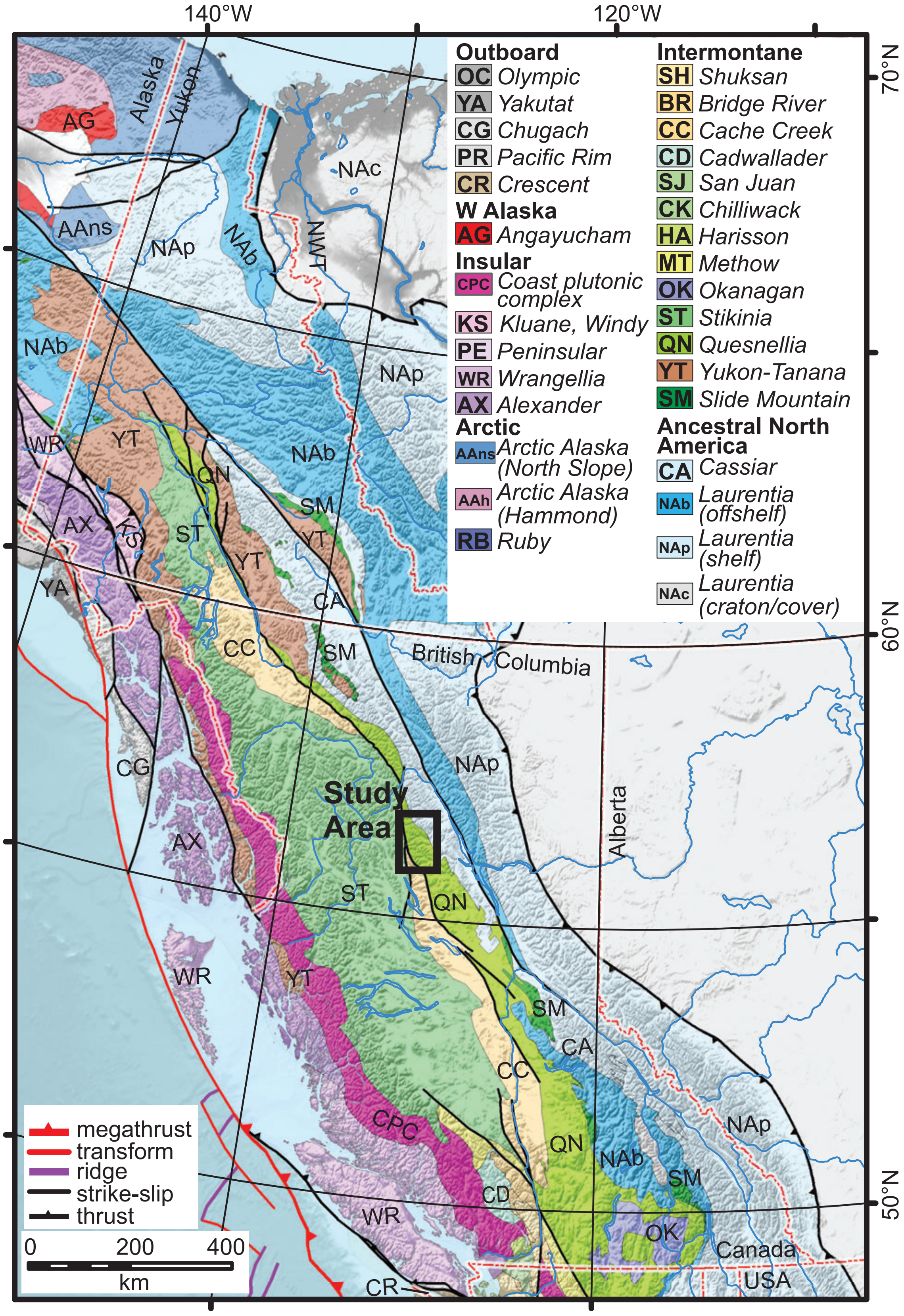

Fig. 1. Location of Hogem batholith study area with respect to Cordilleran terranes of British Columbia. Modified after Colpron and Nelson (2020).

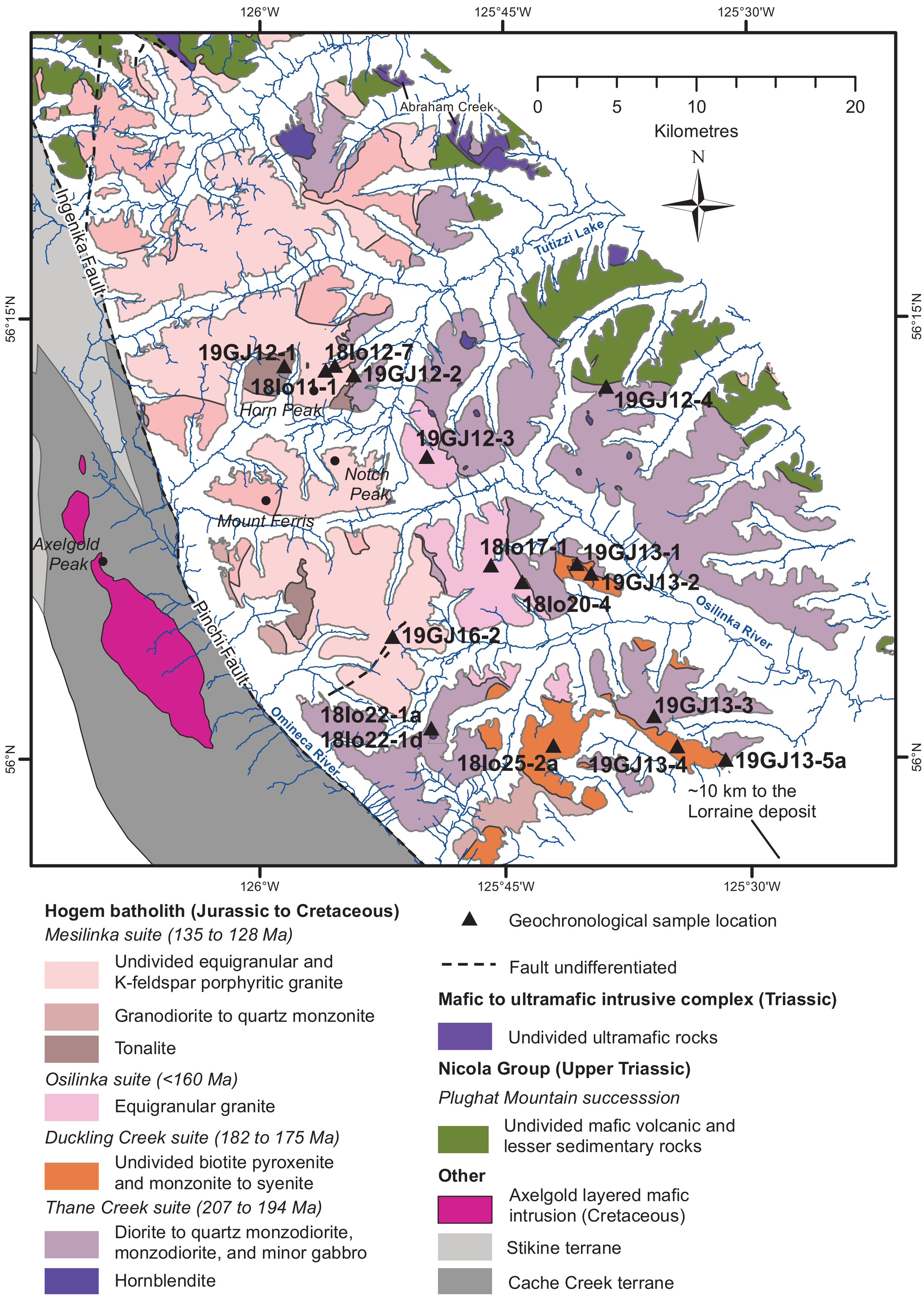

Fig. 2. Geology of northern Hogem batholith with sample locations. After Ootes et al. (2020a,b).

Creek, Duckling Creek, Osilinka, and Mesilinka suites (Fig. 2; Woodsworth, 1976; Schiarizza and Tan, 2005a, b; Devine et al., 2014; Ootes et al., 2019, 2020a-c). Unit descriptions are found in Ootes et al. (2019) and supporting geochemical and geochronological data are in Ootes et al. (2020c) and Jones et al. (2021).

3. Methods

3.1. Sample preparation

Alteration and lichen-free samples were prepared in the field as chips then bagged and sealed. Samples with the prefix 18lo were prepared at the University of British Columbia using standard mineral separation procedures. At the University of Alberta, 1 to 2 kg samples were disaggregated using the electronic pulse disaggregation (EPD) system in the Selective Fragmentation (SELFRAG) laboratory in the Canadian Centre for Isotopic Microanalysis (CCIM). Mineral separates were dried in a 20°C oven, then sieved to pass a 355 µm mesh. The <355 µm fraction was panned to separate high-density minerals, and this portion was dried again in a 20°C oven. A hand-held magnet was used to remove magnetic grains from the high-density minerals. The remaining grains were examined using a stereoscope to select apatite, titanite, and zircon grains for epoxy mounting. Zircon separates from samples with the prefix “18lo” were picked by L. Ootes (British Columbia Geology Survey) and Dr. R. Friedman at the University of British Columbia.

Zircon grain mounts with the prefix “19GJ” were prepared by G. Jones, Dr. R. Stern, and R. Dokken at the Canadian Centre for Isotopic Microanalysis (CCIM), University of Alberta. Apatite and titanite grain mounts were prepared by G. Jones and M. Labbe at the Thin Section Laboratory, Department of Earth and Atmospheric Science, University of Alberta. Minerals were selected and placed onto a mount stage using fine-tipped tweezers, then set with epoxy resin within 25 mm round moulds. Once the epoxy was set, the minerals were polished using diamond grits to expose the grain mid-sections. CL images of each zircon grain mount are in Appendix 2. The sample numbers in the data tables correspond to the rock sample number, followed by a zircon grain identification code that is labeled on the CL images.

3.2. Zircon oxygen-isotope analyses by SIMS

Zircon oxygen isotope (^{18}O/^{16}O) data were collected before further zircon isotope geochemistry by secondary ion mass-spectrometry (SIMS), a non-destructive process. Zircon mounts were first coated with 25 nm of Au, then imaged using a Zeiss EVO MA15 scanning electron microscope (SEM) equipped with cathodoluminescence (CL) and backscattered electron (BSE) detectors. Beam conditions were 15kV and 3-5 nA sample current. Following SEM imaging and before SIMS analysis, a further 100 nm of Au was coated on the grain mount. Zircon grains and individual spots were selected using CL and BSE images of the grains. Grains or zones with fractures, alteration, or metamictization were avoided because these may not yield representative ^{18}O/^{16}O signatures. Most zircons from Hogem batholith display oscillatory zoning and magmatic cores are common; inherited cores are less common. When possible, multiple analytical spots were selected for both the core and rim of a single zircon grain.

^{18}O/^{16}O compositions were measured on 488 spots on 397 zircon grains using a Cameca IMS 1280 multicollector ion microprobe. A ^{133}Cs$^+$ beam was operated using an impact energy of 20 keV and beam current of approximately 2.0 nA. Before data acquisition, the 10 µm diameter was rastered (20 x 20 µm) for 30 seconds, across an area of 5 x 5 µm. The normal incidence electron gun was used for charge compensation. Negative secondary ions were extracted through 10 kV into the secondary (transfer) column. Transfer conditions included a 122 µm entrance slit, a 5 x 5 mm pre-ESA (field) aperture, and 100x (MA80) sample magnification at the field aperture, transmitting all regions of the sputtered area. No energy filtering was employed. The mass/charge separated oxygen ions were detected simultaneously in Faraday cups L’2 (^{16}O$^-$) and H’2 (^{18}O$^-$) as mass resolutions (m/Δm at 10%) of 1950 and 2250, respectively. Secondary ion count rates for ^{16}O$^-$ and ^{18}O$^-$ were approximately $2x10^9$ and $4x10^6$ counts per second using 10^{10} Ω and 10^{11} Ω amplifier circuits, respectively. Faraday cup baselines were determined at the beginning of the analytical run. A single analysis took 240 s in total, including pre-analysis rastering, automated secondary ion tuning, and 75 s of continuous peak counting.

Oxygen isotope results were presented as $\delta^{18}O_{VSMOW}$ and reported in permille, ‰ (Eqn. 1).

$$\delta^{18}O_{VSMOW} = \left(\frac{(^{18}O/^{16}O_{SAMPLE})}{(^{18}O/^{16}O_{VSMOW})} - 1\right) \times 1000 \qquad \text{(Eqn. 1)}$$

where $^{18}O/^{16}O_{VSMOW} = 0.0020052$ (Baertschi, 1976)

Instrumental mass fractionation (IMF) was monitored by repeated analysis of the zircon primary reference material (S0081 with $\delta^{18}O_{VSMOW} = +4.87$‰; R. Stern, unpublished laser fluorination data, University of Oregon), once after every four unknowns. Additionally, a secondary zircon reference material, TEM2 ($\delta^{18}O_{VSMOW} = +8.2$‰; Black et al., 2004) was analyzed after every 12 unknowns. The collective ^{18}O$^-$/^{16}O$^-$ data for S0081 for the single analytical session resulted in a standard deviation of 0.08‰, after correction for systematic within-session drift of +1.5‰. Uncertainties in $\delta^{18}O_{VSMOW}$ of individual spots for the unknowns have a median of ±0.20‰ at 95% confidence, including errors relating to within-spot counting statistics, between-spot (geometric) effects, and correction for IMF. Results for multiple spots on multiple grains of the secondary reference material (TEM2) yield a weighted mean of $\delta^{18}O$ within uncertainty to the accepted value (8.20‰).

3.3. Zircon U-Pb isotopes analyses by LA-ICP-MS and LASS-ICP-MS

Uranium-lead isotopes of zircon grains were determined following oxygen isotope analyses on the same grains. Zircon U-Pb isotope data were collected using laser ablation coupled plasma mass spectrometry (LA-ICP-MS) with a RESOlution 193 nm ArF excimer laser, equipped with a 2-volume Laurin-Technic S-155 ablation cell, coupled with a Thermo Fisher Scientific Element II-XR single collector (SC)-sector field (SF)-ICP-MS in the Arctic Resources Geochemistry Laboratory at the University of Alberta. Analytical points were determined from CL and BSE images, and U-Pb spots were positioned on top of shallow SIMS analysis pits. A 33 µm (session 1-3), 40 µm (session 4), or 23 µm (session 5) diameter laser spot size was ablated using settings of 35 to 50 s of ablation, 50 s of background and washout, 6 Hz repetition rate, 120 mJ laser energy, 11%T attenuator value, and ca. 1.8 J/cm^2 fluence, measured at the ablation site (Table 1). Masses 202, 204, 206, 207, 208, 232, and 238 were measured. Uranium-235 was calculated from ^{238}U results and the ^{238}U/^{235}U isotopic ratio (Jaffey et al., 1971). Data were processed and reduced offline using the Iolite version 3 software package (Paton et al., 2010; Paton et al., 2011), using the data reduction scheme (DRS) 'X_U_Pb_Geochron'. The decay constants of ^{235}U (9.485 x 10^{-10} year^{-1}), ^{238}U (1.55125 x 10^{-10} year^{-1}) and the ^{238}U/^{235}U isotopic ratio (137.88) used in age calculations are from Jaffey et al. (1971).

Uranium-lead isotopes of standard zircon reference material were determined throughout three analytical sessions. Three zircon reference materials were analyzed after every six analyses of unknowns. The natural zircons 91500 (1062.4±0.8 Ma; Wiedenbeck et al., 1995, 2004) or Plešovice (337.13±0.37 Ma; Sláma et al., 2008) were used for the primary calibration reference material to monitor analytical reproducibility, U-Pb fractionation, and instrument drift during each analytical run. The Plešovice, 94-35 (55.5±1.5 Ma; Klepeis et al., 1998), and Mud Tank (731.0±0.2 Ma; Gain et al., 2019) zircons were used as secondary validation reference materials to monitor the accuracy of the primary correction.

A subset of zircons was analyzed using the laser ablation split stream (LASS)-ICP-MS method (Appendix 7), in which U-Pb isotopes were analyzed concomitantly with Lu-Hf on a portion of the same zircon material using separate mass spectrometers. The LASS method used the same ICP-MS and laser set-ups to collect U-Pb as the previously mentioned single-stream ICP-MS method (Table 2).

3.3.1. Filtering

No common Pb correction was applied to the data. The ^{206}Pb/^{204}Pb ratio in the unknown zircons ranged from 200 to 1800000. The presence of significant common Pb in individual zircon analyses was indicated by calculating $f^{206}Pb_c$, in which the ^{206}Pb/^{204}Pb ratio was calculated using the method of Stacey and Kramers (1975) and divided by the measured ^{206}Pb/^{204}Pb ratio for each analysis (e.g., Vezinet et al., 2018). Measured ^{204}Pb was corrected for ^{204}Hg interference by subtracting the counts per second (cps) of ^{202}Hg multiplied by the natural ratio of ^{204}Hg to ^{202}Hg (6.87/29.86; Rosman and Taylor, 1998) from the cps of ^{204}Pb. Zircon with $f^{206}Pb_c$ results >1% (Eqn. 2) were not included in age calculations.

$$f^{206}Pb_c\ \% = [(^{206}Pb/^{204}Pb)_{\text{Stacey \& Kramers, 1975}} / (^{206}Pb/^{204}Pb)_{\text{measured}}] *100 \text{ (Eqn. 2)}$$

Zircon grains with >5% discordance, determined using the individual zircon ^{206}Pb/^{238}U and ^{207}Pb/^{235}U ages, were rejected from intrusive age weighted means. In addition to U-Pb data filters, the internal structures of zircon were examined using CL and BSE images. Xenocrystic or antecrystic cores were identified by the degree of roundness and crosscutting growth zones, and these grains were not used toward calculating sample ages. Zircon grains with suspect age results (significantly younger or older than the main population) that passed the initial data filters were further filtered by removing grains with trace element concentrations of Ca >300 ppm, Fe >300 ppm, Ti >20 ppm, and La >1 ppm. Concentrations greater than these values may indicate altered zircon domains, or growth zones with mineral inclusions, which may affect the interpreted age of the sample. After data filtering, individual zircon ^{206}Pb/^{238}U ages were used to calculate a weighted mean ^{206}Pb/^{238}U age for each sample. Zircon ^{207}Pb/^{235}U and ^{206}Pb/^{238}U ratios were used to determine concordia ages. Weighted means and concordia plots were created using IsoplotR online (Vermeesch, 2018). All reported isotope ratios and age uncertainties are given as 2σ standard error, or 95.4% confidence level, propagated by quadratic addition.

3.4. Zircon Lu-Hf isotopes analyses by LA-ICP-MS and LASS-ICP-MS

Lutetium-hafnium isotopes in zircon were analyzed by multi-collector (MC) LA- ICP-MS at the Arctic Resources Laboratory, the University of Alberta. The same zircon grains used for oxygen and U-Pb isotope analyses were used for Lu-Hf isotope analysis, and the same analytical spots or magmatic zones were sampled. The same laser ablation system used for U-Pb isotope analyses was used for Hf isotope analysis and coupled with a Thermo Fisher Scientific Neptune Plus MC-SF-ICP-MS using multiple Faraday detectors with 10^{11} Ω amplifiers operating in static collection mode. Masses 172, 173, 175, 176, 177, 178, 179, 180, and 181 were measured. A 33 µm diameter laser spot size was ablated using settings of 60 s of ablation, 60 s of background and washout, 8 Hz repetition rate, 120 mJ laser energy, 44%T attenuator value, and ca. 6.5 J/cm^2 (Table 3).

Data were processed and reduced offline using the Iolite version 3 software package (Paton et al., 2010; Paton et al., 2011 and the data reduction scheme (DRS) "Hf_Alberta". Due to the interferences of ^{176}Yb and ^{176}Lu on ^{176}Hf, a two-step correction was necessary to determine accurate Hf isotopic ratios. The Yb-mass bias factor (βYb) was determined using the peak-stripping method, by measuring the ratio of two interference-free isotopes of Yb, ^{172}Yb/^{173}Yb (Woodhead et al., 2004; Fisher et al., 2011), and calculated using the exponential mass fractionation law described in Russell et al. (1978). The measured ^{176}Yb/^{173}Yb was iteratively calibrated to optimize the Yb-interference correction, monitored by zircon reference materials with variable Yb contents (91500, MUN1, MUN3). The Lu interference correction was calculated in the same manner as the Yb interference, assuming that Lu behaves similarly to Yb, using the ^{176}Lu/^{175}Lu ratio (e.g., Vezinet et al., 2018).

The corrected ^{176}Hf/^{177}Hf results of unknowns were converted to εHf(t), which is the ^{176}Hf/^{177}Hf ratio of at the time of crystallization (t) relative to the ^{176}Hf/^{177}Hf ratio of the chondritic uniform reservoir (CHUR; Eqn. 3).

$$\varepsilon Hf_{(t)}= \left(\frac{(^{176}Hf/^{177}Hf_{SAMPLE(t)})}{(^{176}Hf/^{177}Hf_{CHUR(t)})} -1\right) \times 10000 \text{ (Eqn. 3)}$$

in which

$^{176}Hf/^{177}Hf_{(t)} = {}^{176}Hf/^{177}Hf_{(measured)} - {}^{176}Lu/^{177}Hf \text{ x } e^{[(\lambda 176Lu \text{ x } t) - 1]}$, $^{176}Hf/^{177}Hf_{CHUR(measured)}=0.282785\pm1$, $^{176}Lu/^{177}Hf_{CHUR}=0.0336\pm1$ (Bouvier et al., 2008), and $\lambda^{176}Lu=1.867\text{x}10^{-11}$ (Söderlund et al., 2004)

The time of crystallization used in the εHf(t) for individual zircon analyses was either the single zircon ^{206}Pb/^{238}U age, or the interpreted crystallization age of the sample if a single zircon age was unavailable. Uncertainties of εHf(t) values were propagated using the calculations of Ickert (2013).

Table 1. Single stream laser ablation-inductively coupled plasma-mass spectrometry (LA-ICP-MS) parameters for zircon U-Pb analyses.

Laboratory and sample preparation	
Laboratory name	Arctic Resource Lab, University of Alberta (Canada)
Sample type/mineral	Zircon grains (magmatic)
Sample preparation	Conventional mineral separation, polished 1inch resin mount
Imaging	CL & BSE (Zeiss EVO MA15) 15kv, 3-5 nA
Laser ablation system	
Make, Model & type	RESOlution ArF excimer
Ablation cell	Laurin Technic S-155
Laser wavelength	193 nm
Pulse width	4-20 ns
Fluence	*ca*. 1.8 J.cm^{-2} (120 mJ, 11% transmission)
Repetition rate	6 Hz
Ablation/Washout duration	35-50 secs / 50 secs
Ablation rate	0.11-0.15 μm.pulse^{-1}
Spot diameter	33, 40, or 23 μm
Sampling mode / pattern	Static spot ablation
Carrier gas	100% He in the cell, Ar and N$_2$ make-up gas combined using a Y-piece 50% along the sample transport line to the torch.
Cell carrier gas flow	A mixture of 1.6-1.8 L/min Ar and 12-14ml/min N$_2$, which entered tangentially from the top of the S-155 ablation cell funnel and ~800 ml/min He entering from the side of the cell
ICP-MS instruments	
U–Th–Pb measurements	
Make, Model & type	Thermo Fisher Scientific, Element XR, SC-SF-ICP-MS
Sample introduction	Ablation aerosol introduced through Tygon tubing
RF power	1360W
Detection system	202, 208, 232 in triple mode. 206 and 238 in analogue mode. 204 and 207 in counting mode 235 is calculated using canonical value. No Faraday cup used.
Masses measured	202, 204, 206, 207, 208, 232, 238
Integration time per peak/ dwell times	30 ms on 202, 204, 208 and 232; 60 ms on 206, 207 and 238
Total integration time	300 ms for each output datapoint
IC Dead time	20 ns
Data processing	
Gas blank	30 second on-peak zero subtracted both for U-Pb and Lu-Hf measurements
Calibration strategy	91500 or Plešovice used as primary reference material (U-Pb), Plešovice, 94-35, Mud Tank used as secondaries/validation materials.
Reference Material info	Plešovice (Sláma et al., 2008) 91500 (Wiedenbeck et al., 1995; Wiedenbeck et al., 2004; Blichert-Toft, 2008) Mud Tank (Gain et al., 2019) 94-35 (Klepeis et al., 1998)
Data processing package used / Correction for LIEF	Iolite software package (Paton et al., 2010; Paton et al., 2011; Fisher et al., 2017) using the following DRS: "X_U_Pb Geochron" for U–Th–Pb isotope analyses. LIEF correction assumes matrix match between reference material and samples.
Mass discrimination	Standard-sample bracketing with ^{207}Pb/^{206}Pb and ^{206}Pb/^{238}U normalized to primary reference material.
Common-Pb correction, composition and uncertainty	No common-Pb correction applied to the data
Uncertainty level & propagation	Ages are quoted at a coverage factor of 2, absolute. Propagation is by quadratic addition. Reproducibility and age uncertainty of reference material and common-Pb composition uncertainty are propagated where appropriate.

Table 2. Split stream laser ablation-inductively coupled plasma-mass spectrometry (LASS-ICP-MS) parameters for zircon U-Pb and Lu-Hf analyses.

Laboratory and sample preparation	
Laboratory name	Arctic Resource Lab, University of Alberta (Canada)
Sample type/mineral	Zircon grains (magmatic)
Sample preparation	Conventional mineral separation, polished 1inch resin mount
Imaging	CL & BSE (Zeiss EVO MA15) 15kv, 3-5 nA
Laser ablation system	
Make, Model & type	RESOlution ArF excimer
Ablation cell	Laurin Technic S-155
Laser wavelength	193 nm
Pulse width	4-20 ns
Fluence	ca. 6 J.cm^{-2} (120 mJ, 44% transmission)
Repetition rate	8 Hz
Ablation/Washout duration	45 secs / 45 secs
Ablation rate	0.125μm.pulse^{-1} with the *ca*. 6.5 J.cm^{-2} setting
Spot diameter	44 μm
Sampling mode / pattern	Static spot ablation
Carrier gas	100% He in the cell, Ar and N$_2$ make-up gas combined using a Y-piece 50% along the sample transport line to the torch.
Cell carrier gas flow	A mixture of 1.6-1.8 L/min Ar and 12-14ml/min N$_2$, which entered tangentially from the top of the S-155 ablation cell funnel and ~800 ml/min He entering from the side of the cell
ICP-MS instruments	
U–Th–Pb measurements	
Make, Model & type	Thermo Fisher Scientific, Element XR, SC-SF-ICP-MS
Sample introduction	Ablation aerosol introduced through Tygon tubing
RF power	1360W
Detection system	202, 208, 232 in triple mode. 206 and 238 in analogue mode. 204 and 207 in counting mode 235 is calculated using canonical value. No Faraday cup used.
Masses measured	202, 204, 206, 207, 208, 232, 238
Integration time per peak/ dwell times	30 ms on 202, 204, 208 and 232; 60 ms on 206, 207 and 238
Total integration time	300 ms for each output datapoint
IC Dead time	20 ns
	Lu–Yb–Hf measurements
Make, Model & type	Thermo Fisher Scientific, Neptune Plus, MC-SF-ICP-MS
Sample introduction	Ablation aerosol introduced tygon tubing. Ni-Jet Sample cone and X-Skimmer cone.
RF power	1250W
Detection system	Static Faraday (attached to 10^{11} Ω amplifier) measurement
Masses measured	172, 173, 175, 176, 177, 178, 179, 180, 181
Total integration time per output datapoint	1.049 secs
Cup configuration	L4 L3 L2 L1 Axial H1 H2 H3 H4 172 173 175 176 177 178 179 180 181
Data processing	
Gas blank	30 second on-peak zero subtracted both for U-Pb and Lu-Hf measurements
Calibration strategy	91500 used as primary reference material (U-Pb), Plešovice, GJ-1, MUN1 & MUN-3 used as secondaries/validation materials.
Reference Material info	GJ-1 (Jackson et al., 2004; Morel et al., 2008) Plešovice (Sláma et al., 2008) MUN-1 and MUN-3 (Fisher et al., 2011) 91500 (Wiedenbeck et al., 1995; Wiedenbeck et al., 2004; Blichert-Toft, 2008)
Data processing package used / Correction for LIEF	Iolite software package (Paton et al., 2010; Paton et al., 2011; Fisher et al., 2017) using the following DRS: "U_Pb Geochron 4" for U–Th–Pb isotope analyses';

Table 2, continued.

	“*Hf_Alberta*” for Lu-Hf isotope analyses. LIEF correction assumes matrix matcl between reference material and samples.
Mass discrimination	Standard-sample bracketing with ^{207}Pb/^{206}Pb and ^{206}Pb/^{238}U normalized t primary reference material.
Common-Pb correction, composition and uncertainty	No common-Pb correction applied to the data
Yb mass bias coefficient (β^{Yb})	Calculated using ^{173}Yb/^{172}Yb invariant ratio and the exponential law of Russel et al. (1978).
Yb interference	Calculated with ^{176}Yb/^{173}Yb ratio, the Yb-mass bias coefficient (β^{Yb}) and th exponential law of Russell et al. (1978). Daily adjusted.
Lu interference	Calculated with ^{176}Lu/^{175}Lu ratio, the Yb-mass bias coefficient (β^{Yb}) and th exponential law of Russell et al. (1978). Daily adjusted.
Uncertainty level & propagation	Ages are quoted at a coverage factor of 2, absolute. Propagation is by quadrati addition. Reproducibility and age uncertainty of reference material and common Pb composition uncertainty are propagated where appropriate.

Hafnium isotopes of standard zircon reference material were determined throughout three analytical sessions. Four zircon reference materials were analyzed after every seven to twelve unknown analyses. The natural zircon Plešovice (^{176}Hf/^{177}Hf=0.282482±13; Sláma et al., 2008) was used as the primary calibration reference material to monitor analytical reproducibility, Hf fractionation, and instrument drift during each analytical run. The natural zircon 91500 (^{176}Hf/^{177}Hf=0.282308±6; Wiedenbeck et al., 1995; Blichert-Toft, 2008) and synthetic zircons MUN1 and MUN3 (^{176}Hf/^{177}Hf=0.282135±7; Fisher et al., 2011) were used as secondary reference materials to verify the accuracy of the calibration. The weighted mean ^{176}Hf/^{177}Hf results for the primary and secondary zircon reference materials were compared to the accepted values.

A subset of zircons was analyzed using the laser ablation split stream (LASS)-ICP-MS method (Appendices 7 and 8), in which Lu-Hf and U-Pb or trace elements were analyzed concomitantly on a portion of the same zircon material using separate mass spectrometers (Tables 2 and 4). The LASS method used the same ICP-MS and laser set-ups to collect U-Pb as the previously mentioned single-stream ICP-MS method.

3.5. Zircon trace element analyses by LA-ICP-MS and LASS-ICP-MS

Trace elements in zircon were analyzed by LA-SC-SF-ICP-MS with the same laser ablation and ICP-MS configuration used for U-Pb isotope analyses. The same zircon grains used for oxygen, U-Pb, and Hf isotope analyses were used for trace element analysis, and the same analytical spots or growth zones were sampled. A portion of the samples were analyzed for Hf isotopes before trace element analysis, while the other portion was analyzed for trace elements first. Concentrations for twenty-nine elements were acquired: ^{31}P, ^{43}Ca, ^{45}Sc, ^{49}Ti, ^{55}Mn, ^{57}Fe, ^{89}Y, ^{93}Nb, ^{137}Ba, ^{139}La, ^{140}Ce, ^{141}Pr, ^{146}Nd, ^{147}Sm, ^{153}Eu, ^{157}Gd, ^{159}Tb, ^{163}Dy, ^{165}Ho, ^{166}Er, ^{169}Tm, ^{172}Yb, ^{175}Lu, ^{177}Hf, ^{181}Ta, ^{232}Th, ^{204}Pb, ^{208}Pb, and ^{238}U. Samples were ablated for 40 or 50s, using a 33µm or 50 µm laser beam diameter, 60s of background and washout, 10 Hz repetition rate, 120mJ laser energy, 26%T attenuator value, and fluence of ca. 3.5 J/cm^2 (Table 5).

Data were processed and reduced offline using the Iolite version 4.3.7 software package (Paton et al., 2010; Paton et al., 2011) and the DRS “Trace Elements” (Longerich et al., 1996). Trace element reference materials were analyzed between every 8-10 unknowns. Glass standard reference material (SRM) NIST 612 was used as the primary calibration standard. NIST SRM 614 and zircon 91500 were used as secondary verification standards to monitor accuracy, instrumental drift, and matrix effects. The stoichiometric ^{29}Si content in zircon (15.32 wt.%) was used as an internal standard. Limits of detection (LOD= 3.29σ blank; Currie, 1968) were calculated in Iolite using the calculation of Pettke et al. (2012), based on Poisson statistics. For data to be quantitative they must exceed the limit of quantification (LOQ= 10σ blank; Currie, 1968), which was calculated and reported for each analysis.

A subset of zircons was analyzed using the laser ablation split stream (LASS)-ICP-MS method (Appendix 8), in which trace elements and Lu-Hf isotopes were analyzed concomitantly on a portion of the same zircon material using separate mass spectrometers. The LASS method used the same ICP-MS and laser setups to collect trace elements as the single-stream ICP-MS method (Table 4).

3.6. Apatite and titanite Sm-Nd and U-Pb isotope analyses by LASS-ICP-MS

Samarium-neodymium and U-Pb isotopes in apatite and titanite were simultaneously measured using the laser ablation split-stream (LASS)-ICP-MS method (e.g., Fisher et al., 2014). Concurrent Sm-Nd and U-Pb measurements were obtained at the University of Alberta Arctic Resources Laboratory, using the same laser and ICP-MS configurations described in the U-Pb and Lu-Hf single stream LA-ICP-MS methods. The U-Pb isotope measurements were acquired on a Thermo Fisher Element II XR SC-SF-ICP-MS. The Sm-Nd isotope measurements were obtained simultaneously, on a portion of the same material as analyzed for U-Pb, on a Thermo Fisher Scientific Neptune Plus MC-SF-ICP-MS using multiple Faraday detectors with 10^{11} Ω amplifiers operating in static collection mode. Masses 143, 144, 145, 148, and 150 were measured. The apatite and titanite samples were ablated using a RESOlution 193 nm ArF excimer laser using a 90 µm diameter spot size, 45s of ablation time, 60s of background and washout, 8 Hz repetition rate, and ca. 5-6 J/cm^2 fluence (Table 6).

Data were processed and reduced offline using the Iolite version 3 software package (Paton et al., 2010; Paton et al., 2011) in multiple DRS mode, using the DRS “SmNd_Downhole”

Table 3. Single stream laser ablation-inductively coupled plasma-mass spectrometry (LA-ICP-MS) parameters for zircon Lu-Hf analyses.

<table>
<tr><th colspan="10">Laser ablation system</th></tr>
<tr><td>Make, Model & type</td><td colspan="9">RESOlution ArF excimer</td></tr>
<tr><td>Ablation cell</td><td colspan="9">Laurin Technic S-155</td></tr>
<tr><td>Laser wavelength</td><td colspan="9">193 nm</td></tr>
<tr><td>Pulse width</td><td colspan="9">20 ns</td></tr>
<tr><td>Fluence</td><td colspan="9">ca. 6 J.cm^{-2} (120 mJ, 44% transmission)</td></tr>
<tr><td>Repetition rate</td><td colspan="9">8 Hz</td></tr>
<tr><td>Ablation/Washout duration</td><td colspan="9">60 secs / 60 secs</td></tr>
<tr><td>Ablation rate</td><td colspan="9">0.07μm.pulse^{-1}</td></tr>
<tr><td>Spot diameter</td><td colspan="9">33 μm</td></tr>
<tr><td>Sampling mode / pattern</td><td colspan="9">Static spot ablation</td></tr>
<tr><td>Carrier gas and gas flow</td><td colspan="9">A mixture of ~0.85 L/min Ar and 6- 7 ml/min N$_2$, which entered tangentially from the top of the S-155 ablation cell funnel and ~400 ml/min He entering from the side of the cell.</td></tr>
<tr><th colspan="10">Lu–Yb–Hf measurements</th></tr>
<tr><td>Make, Model & type</td><td colspan="9">Thermo Fisher Scientific, Neptune Plus, MC-SF-ICP-MS</td></tr>
<tr><td>Sample introduction</td><td colspan="9">Ablation aerosol introduced tygon tubing.
Ni-Jet Sample cone and X-Skimmer cone.</td></tr>
<tr><td>RF power</td><td colspan="9">1250W</td></tr>
<tr><td>Detection system</td><td colspan="9">Static Faraday (attached to 10^{11} Ω amplifier) measurement</td></tr>
<tr><td>Masses measured</td><td colspan="9">172, 173, 175, 176, 177, 178, 179, 180, 181</td></tr>
<tr><td>Total integration time per output datapoint</td><td colspan="9">1.049 secs</td></tr>
<tr><td rowspan="2">Cup configuration</td><td>L4</td><td>L3</td><td>L2</td><td>L1</td><td>Axial</td><td>H1</td><td>H2</td><td>H3</td><td>H4</td></tr>
<tr><td>172</td><td>173</td><td>175</td><td>176</td><td>177</td><td>178</td><td>179</td><td>180</td><td>181</td></tr>
<tr><th colspan="10">Data processing</th></tr>
<tr><td>Gas blank</td><td colspan="9">60 second on-peak zero subtracted for Lu-Hf measurements</td></tr>
<tr><td></td><td colspan="9"></td></tr>
<tr><td>Reference Material info</td><td colspan="9">Plešovice (Sláma et al., 2008)
91500 (Blichert-Toft, 2008)
MUN-1 and MUN-3 (Fisher et al., 2011)</td></tr>
<tr><td>Data processing package used</td><td colspan="9">Iolite software package (Paton *et al.*, 2010; Paton *et al.*, 2011; Fisher *et al.*, 2017) using the following DRS: ““*Hf_Alberta*”</td></tr>
<tr><td>Yb mass bias coefficient (β^{Yb})</td><td colspan="9">Calculated using ^{173}Yb/^{172}Yb invariant ratio and the exponential law of Russell et al. (1978).</td></tr>
<tr><td>Yb interference</td><td colspan="9">Calculated with ^{176}Yb/^{173}Yb ratio, the Yb-mass bias coefficient (β^{Yb}) and the exponential law of Russell et al. (1978). Daily adjusted.</td></tr>
<tr><td>Lu interference</td><td colspan="9">Calculated with ^{176}Lu/^{175}Lu ratio, the Yb-mass bias coefficient (β^{Yb}) and the exponential law of Russell et al. (1978). Daily adjusted.</td></tr>
<tr><td></td><td colspan="9"></td></tr>
</table>

and “X_U_Pb_Geochron”. The Nd mass bias corrections were calibrated using the Bear Lake titanite (1047.1±0.4 Ma; ^{143}Nd/^{144}Nd=0.512310±5; TH-tnt-1 of Fisher et al., 2020 and BLR-1 of Aleinikoff et al., 2007) and Bancroft apatite (1021±3 Ma; ^{143}Nd/^{144}Nd=0.512048±6; TH-ap-1 of Fisher et al., 2020) as primary reference materials. Verification of the Nd mass bias correction was determined using the MKED titanite (1519.5±3.0 Ma; ^{143}Nd/^{144}Nd=0.511630±3; Spandler et al., 2016) and MAD apatite (475.4±1.8 Ma; ^{143}Nd/^{144}Nd=0.511304±13; Fisher et al., 2020). The U-Pb mass bias corrections were calibrated using the MKED titanite and Bancroft apatite and verified using the Bear Lake titanite and MAD apatite. The LASS-ICP-MS ^{143}Nd/^{144}Nd and U-Pb ages were compared to the reported values for each reference material.

The ^{143}Nd/^{144}Nd results of unknown titanite and apatite grains were converted to εNd$_{(t)}$, which is the ^{143}Nd/^{144}Nd ratio of at the time of crystallization (t) relative to the ^{143}Nd/^{144}Nd ratio of the chondritic uniform reservoir (CHUR; Eqn. 4).

$$\varepsilon\text{Nd}_{(t)} = \left(\frac{(^{143}\text{Nd}/^{144}\text{Nd}_{\text{SAMPLE(t)}})}{(^{143}\text{Nd}/^{144}\text{Nd}_{\text{CHUR(t)}})} - 1\right) \times 10000 \quad \text{(Eqn. 4)}$$

in which

^{143}Nd/^{144}Nd$_{(t)}$= ^{143}Nd/^{144}Nd$_{(\text{measured})}$ – ^{147}Sm/^{144}Nd x e$^{[(\lambda 147\text{Sm x t) - 1]}}$, ^{143}Nd/^{144}Nd$_{\text{CHUR(measured)}}$=0.51263±11, ^{147}Sm/^{144}Nd$_{\text{CHUR}}$=0.1960±4 (Bouvier et al., 2008), and λ^{147}Sm=6.54x10^{-12} (Lugmair and Marti, 1979)

The interpreted titanite U-Pb discordia age was used for time of crystallization in the εNd$_{(t)}$ calculation for individual titanite analyses. Because apatite U-Pb analyses did not yield any ages, the interpreted zircon ^{206}Pb/^{238}U ages from the same samples were used to calculate εNd$_{(t)}$ of the apatite grains. Uncertainties on εNd$_{(t)}$ values were propagated using the calculations of Ickert (2013).

Additionally, titanite and apatite εNd$_{(t)}$ results were converted to εHf$_{(t)}$ using the calculation of Vervoort et al. (2011), which

Table 4. Split stream laser ablation-inductively coupled plasma-mass spectrometry (LASS-ICP-MS) parameters for zircon Lu-Hf and trace elements analyses.

<table>
<tr><th colspan="10">Laboratory and sample preparation</th></tr>
<tr><td>Laboratory name</td><td colspan="9">Arctic Resource Lab, University of Alberta (Canada)</td></tr>
<tr><td>Sample type/mineral</td><td colspan="9">Zircon grains (magmatic)</td></tr>
<tr><td>Sample preparation</td><td colspan="9">Conventional mineral separation, polished 1inch resin mount</td></tr>
<tr><td>Imaging</td><td colspan="9">CL & BSE (Zeiss EVO MA15)
15kv, 3-5 nA</td></tr>
<tr><th colspan="10">Laser ablation system</th></tr>
<tr><td>Make, Model & type</td><td colspan="9">RESOlution ArF excimer</td></tr>
<tr><td>Ablation cell</td><td colspan="9">Laurin Technic S-155</td></tr>
<tr><td>Laser wavelength</td><td colspan="9">193 nm</td></tr>
<tr><td>Pulse width</td><td colspan="9">4-20 ns</td></tr>
<tr><td>Fluence</td><td colspan="9">ca. 6 J.cm^{-2} (120 mJ, 44% transmission)</td></tr>
<tr><td>Repetition rate</td><td colspan="9">8 Hz</td></tr>
<tr><td>Ablation/Washout duration</td><td colspan="9">60 secs / 60 secs</td></tr>
<tr><td>Ablation rate</td><td colspan="9">~0.075 μm.pulse^{-1}</td></tr>
<tr><td>Spot diameter</td><td colspan="9">33 or 40 μm</td></tr>
<tr><td>Sampling mode / pattern</td><td colspan="9">Static spot ablation</td></tr>
<tr><td>Carrier gas</td><td colspan="9">100% He in the cell, Ar and N_2 make-up gas combined using a Y-piece 50% along the sample transport line to the torch.</td></tr>
<tr><td>Cell carrier gas flow</td><td colspan="9">A mixture of 1.6-1.8 L/min Ar and 12-14ml/min N_2, which entered tangentially from the top of the S-155 ablation cell funnel and ~800 ml/min He entering from the side of the cell</td></tr>
<tr><th colspan="10">ICP-MS instruments</th></tr>
<tr><td></td><td colspan="9">Lu–Yb–Hf measurements</td></tr>
<tr><td>Make, Model & type</td><td colspan="9">Thermo Fisher Scientific, Neptune Plus, MC-SF-ICP-MS</td></tr>
<tr><td>Sample introduction</td><td colspan="9">Ablation aerosol introduced tygon tubing.
Ni-Jet Sample cone and X-Skimmer cone.</td></tr>
<tr><td>RF power</td><td colspan="9">1250W</td></tr>
<tr><td>Detection system</td><td colspan="9">Static Faraday (attached to 10^{11} Ω amplifier) measurement</td></tr>
<tr><td>Masses measured</td><td colspan="9">172, 173, 175, 176, 177, 178, 179, 180, 181</td></tr>
<tr><td>Total integration time per output datapoint</td><td colspan="9">1.049 secs</td></tr>
<tr><td rowspan="2">Cup configuration</td><td>L4</td><td>L3</td><td>L2</td><td>L1</td><td>Axial</td><td>H1</td><td>H2</td><td>H3</td><td>H4</td></tr>
<tr><td>172</td><td>173</td><td>175</td><td>176</td><td>177</td><td>178</td><td>179</td><td>180</td><td>181</td></tr>
<tr><td></td><td colspan="9">Trace elements measurements</td></tr>
<tr><td>Make, Model & type</td><td colspan="9">Thermo Fisher Scientific, Element XR, SC-SF-ICP-MS</td></tr>
<tr><td>Sample introduction</td><td colspan="9">Ablation aerosol introduced through Tygon tubing</td></tr>
<tr><td>RF power</td><td colspan="9">1360W</td></tr>
<tr><td>Elements measured</td><td colspan="9">^{31}P, ^{43}Ca, ^{45}Sc, ^{49}Ti, ^{55}Mn, ^{57}Fe, ^{89}Y, ^{93}Nb, ^{137}Ba, ^{139}La, ^{140}Ce, ^{141}Pr, ^{146}Nd, ^{147}Sm, ^{153}Eu, ^{157}Gd, ^{159}Tb, ^{163}Dy, ^{165}Ho, ^{166}Er, ^{169}Tm, ^{172}Yb, ^{175}Lu, ^{177}Hf, ^{181}Ta, ^{232}Th, ^{204}Pb, ^{208}Pb, and ^{238}U</td></tr>
<tr><th colspan="10">Data processing</th></tr>
<tr><td>Calibration strategy</td><td colspan="9">Plešovice used as primary reference material (Lu-Hf), 91500, MUN1 & MUN-3 used as secondaries/validation materials.
NIST SRM 612 used as primary reference material (trace elements), NIST SRM 614 and zircon 91500 used as secondaries/validation materials. Stoichiometric ^{29}Si content in zircon (15.32 wt.%) used as an internal standard.</td></tr>
<tr><td>Reference Material info</td><td colspan="9">Plešovice (Sláma et al., 2008)
MUN-1 and MUN-3 (Fisher et al., 2011)
NIST SRM 612 (Jochum et al., 2011)
NIST SRM 614 (Jochum et al., 2011)
Zircon 91500 (Wiedenbeck et al., 2004)
91500 (Wiedenbeck et al., 1995; Wiedenbeck et al., 2004; Blichert-Toft, 2008)</td></tr>
<tr><td>Data processing package used / Correction for LIEF</td><td colspan="9">Iolite software package (Paton et al., 2010; Paton et al., 2011; Fisher et al., 2017) using the following DRS: “<i>Hf_Alberta</i>” for Lu-Hf isotope analyses; “<i>X_Trace Elements_IS</i>” for trace elements analysis. LIEF correction assumes matrix match between reference material and samples.</td></tr>
<tr><td>Yb mass bias coefficient (β^{Yb})</td><td colspan="9">Calculated using ^{173}Yb/^{172}Yb invariant ratio and the exponential law of Russell et al. (1978).</td></tr>
</table>

Table 4 contined.

Yb interference	Calculated with ^{176}Yb/^{173}Yb ratio, the Yb-mass bias coefficient (β^{Yb}) and the exponential law of Russell et al. (1978). Daily adjusted.
Lu interference	Calculated with ^{176}Lu/^{175}Lu ratio, the Yb-mass bias coefficient (β^{Yb}) and the exponential law of Russell et al. (1978). Daily adjusted.
Uncertainty level & propagation	Uncertainties are quoted at a coverage factor of 2, absolute. Propagation is by quadratic addition. Limits of detection were determined using calculations (Pettke et al., 2012) in Iolite (Paton et al., 2010; Paton et al., 2011).

uses the linearity of the mantle Hf-Nd isotope array (Eqn. 5).

$$\varepsilon\mathrm{Hf}_{(t)} = [1.55\ \mathrm{x}\ \varepsilon\mathrm{Nd}_{(t)}] + 1.21 \quad \text{(Eqn. 5)}$$

4. Results

4.1. SIMS zircon oxygen-isotope results

Igneous zircon $\delta^{18}O_{VSMOW}$ results are in Appendix 3. The $\delta^{18}O$ results of Hogem batholith zircons are compared to the approximate $\delta^{18}O$ range of zircons sourced from the mantle ($\delta^{18}O$=+5.3±0.6‰; Valley et al., 1998). Zircons with $\delta^{18}O$ values higher than the mantle range indicate possible interaction with the low-temperature hydrosphere (i.e., crust that interacted with the hydrosphere, was buried, and then later melted) whereas sub-mantle $\delta^{18}O$ values suggest high-temperature hydrothermal zircon sources (Valley et al., 2005). Thane Creek zircon $\delta^{18}O$ compositions range from +4.95 to +8.52‰, with most (n=170/177) between +5.00 and +6.50‰. Duckling Creek zircon $\delta^{18}O$ compositions range from +5.48 to +6.72‰ with most (n=77/84) between +6.00 and +6.72‰. Osilinka zircon $\delta^{18}O$ compositions range from +4.11 to +13.45‰, but predominantly (n=41/63) from +5.00 to +6.00‰. Because most Osilinka suite zircons are interpreted as inherited, these $\delta^{18}O$ values represent the oxygen-isotope composition(s) of the primary magma source(s). Mesilinka zircon $\delta^{18}O$ compositions range from +4.68 to +12.22‰. There are two main distributions of zircon $\delta^{18}O$, with values from +5.00 to 6.00‰ (n=69/164) and from +7.00 to 8.00‰ (n=72/164).

4.2. LA-ICP-MS and LASS-ICP-MS zircon U-Pb results

Zircon LA- and LASS-ICP-MS U-Pb isotope data are reported in Appendices 4 and 7. These results include new ages and refined interpretations of previously reported ages (Ootes et al., 2020c).

4.2.1. Thane Creek hornblendite: 18lo22-1a (previously reported in Ootes et al. (2020c)

Hornblendite sample 18lo22-1a of the Thane Creek suite is from 18.6 km south-southeast of Mount Ferris (Fig. 2). It is a coarse-grained to pegmatitic plagioclase-bearing hornblendite. Pegmatitic white amphibole-plagioclase segregations (7%) are interstitial to predominantly green amphibole (72%). Amphibole is commonly overgrown by brown or green biotite, with biotite making up 10% of the sample. The sample contains 5% magnetite that is interstitial to amphibole and is concentrated with accessory titanite (1%) and apatite (trace). Coarse, subhedral accessory epidote (2%) occurs in pegmatitic plagioclase segregations. Euhedral, ~100 to 200 µm long zircon (trace) grains occur within patches of intercumulus feldspar and epidote. Trace fine-grained chalcopyrite is disseminated through the sample.

The sample was analyzed by single stream LA-ICP-MS. After analysis and data filtering, the resulting weighted mean ^{206}Pb/^{238}U age is 191.4±0.7 Ma (n=33/42; MSWD=0.87; pof=0.68). A zircon CA-TIMS U-Pb age of 197.6±0.1 Ma for sample 18lo22-1a was previously determined (Ootes et al., 2020b). The discrepancy between the LA-ICP-MS weighted mean ^{206}Pb/^{238}U date (191.4±0.7 Ma) and the reported CA-TIMS ^{206}Pb/^{238}U date (197.6±0.1 Ma) may be due to differences in the calibration techniques between the LA-ICP-MS and CA-TIMS methods. Although both the LA-ICP-MS and CA-TIMS U-Pb dates of the hornblendite are considered valid, the CA-TIMS date (197.6±0.1 Ma) is interpreted to be more accurate and the best estimate of the crystallization age.

4.2.2. Thane Creek Quartz diorite: 18lo22-1d (revision of result in Ootes et al. (2020b,c)

Quartz diorite sample 18lo22-1d of the Thane Creek suite is from 18.6 km south-southeast of Mount Ferris, approximately 100 m east of hornblendite sample 18lo22-1a (Fig. 2). It is a "salt and pepper", medium-grained equigranular quartz diorite. The rock is deformed and contains a moderate foliation defined by plagioclase, biotite, and amphibole. The sample is mostly clay-altered plagioclase (65%), biotite (12%), and amphibole (6%). Minor clay-altered alkali feldspar (7%) and quartz (1-2%) are present and interstitial to plagioclase. Accessory anhedral to subhedral, fine-grained epidote, apatite, magnetite, and zircon spatially occur with biotite. Trace fine-grained chalcopyrite is disseminated through the sample.

The sample was analyzed by single stream LA-ICP-MS. After analysis and data filtering, the resulting weighted mean ^{206}Pb/^{238}U age is 199.0±0.5 Ma (n=26/46; MSWD=1.2; pof=0.24) and is interpreted as the crystallization age for sample 18lo22-1d.

A zircon CA-TIMS age of 196.61±0.19 Ma was previously determined for sample 18lo22-1d (Ootes et al., 2020b). The CA-TIMS age was interpreted using the youngest zircon result out of five grains, which range in ^{206}Pb/^{238}U age from 196.61±0.19 to 202.28±0.64 Ma (Ootes et al., 2020b). Although the CA-TIMS U-Pb age results are more precise than LA-ICP-MS U-Pb age results for individual zircon grains, the range of LA-ICP-MS ages agree with the range of CA-TIMS U-Pb results for sample 18lo22-1d. The reported CA-TIMS age may not represent the main stage of zircon crystallization in this sample, because the youngest zircon may have crystallized later than the bulk of the population. The LA-ICP-MS age takes a greater range of dates into account and is more representative of the age range of the zircon population in this sample than the interpreted CA-TIMS age. We consider the LA-ICP-MS age (199.0±0.5 Ma) the best estimate of the crystallization age for quartz diorite sample 18lo22-1d.

Table 5. Single stream laser ablation-inductively coupled plasma-mass spectrometry (LA-ICP-MS) parameters for zircon trace elements analyses.

Laboratory and sample preparation	
Laboratory name	Arctic Resource Lab, University of Alberta (Canada)
Sample type/mineral	Zircon grains (magmatic)
Sample preparation	Conventional mineral separation, polished 1 inch resin mount
Imaging	CL & BSE (Zeiss EVO MA15) 15kv, 3-5 nA
Laser ablation system	
Make, Model & type	RESOlution ArF excimer
Ablation cell	Laurin Technic S-155
Laser wavelength	193 nm
Pulse width	4-20 ns
Fluence	3.5 J.cm^{-2} (120 mJ, 26% transmission)
Repetition rate	10 Hz
Ablation/Washout duration	60 secs / 60 secs
Ablation rate	0.06 or 0.08 μm.pulse^{-1}
Spot diameter	33 or 50 μm
Sampling mode / pattern	Static spot ablation
Carrier gas	A mixture of ~0.85 L/min Ar and 1ml/min N$_2$, which entered tangentially from the top of the S-155 ablation cell funnel and ~350 ml/min He entering from the side of the cell.
ICP-MS instruments	
Trace elements measurements	
Make, Model & type	Thermo Fisher Scientific, Element XR, SC-SF-ICP-MS
Sample introduction	Ablation aerosol introduced through Tygon tubing
RF power	1360W
Make-up gas flow (l/min)	Total gas is made of ~1.6 l.min^{-1} of Ar, 0.8-0.9 l.min^{-1} of He and 12-14 ml.min^{-1} of N$_2$. This total gas is divided between both ICP-MS at a ~ 50-50 rate.
Elements measured	^{31}P, ^{43}Ca, ^{45}Sc, ^{49}Ti, ^{55}Mn, ^{57}Fe, ^{89}Y, ^{93}Nb, ^{137}Ba, ^{139}La, ^{140}Ce, ^{141}Pr, ^{146}Nd, ^{147}Sm, ^{153}Eu, ^{157}Gd, ^{159}Tb, ^{163}Dy, ^{165}Ho, ^{166}Er, ^{169}Tm, ^{172}Yb, ^{175}Lu, ^{177}Hf, ^{181}Ta, ^{232}Th, ^{204}Pb, ^{208}Pb, and ^{238}U
Data Processing	
Calibration strategy	NIST SRM 612 used as primary reference material, NIST SRM 614 and zircon 91500 used as secondaries/validation materials. Stoichiometric ^{29}Si content in zircon (15.32 wt.%) used as an internal standard.
Reference Material info	NIST SRM 612 (Jochum et al., 2011) NIST SRM 614 (Jochum et al., 2011) Zircon 91500 (Wiedenbeck et al., 2004)
Data processing package used	Iolite software package (Paton et al., 2010; Paton et al., 2011) using the following DRS: "*Trace Elements*" (Longerich et al., 1996).
Uncertainty level & limits of detection	Concentrations are quoted at a coverage factor of 2, absolute. Limits of detection were determined using calculations (Pettke et al., 2012) in Iolite (Paton et al., 2010; Paton et al., 2011).

4.2.3. Thane Creek quartz diorite: 19GJ12-4 (revision of result in Ootes et al. (2020c)

Quartz diorite sample 19GJ12-4 of the Thane Creek suite is from 17.9 km east-northeast of Notch Peak (Fig. 2). It is a white and black, medium-grained, equigranular quartz diorite, and is composed of mostly plagioclase (62%), with about 25% equal parts green amphiboles with corroded clinopyroxene cores, and brown (metamorphic?) and green biotite. The sample contains minor quartz (6%) and alkali feldspar (7%), with accessory magnetite, apatite, titanite, zircon, and epidote. Titanite occurs as rims on magnetite grains. Euhedral, fine-grained apatite (trace) are included in feldspar, magnetite, and amphibole. Epidote occurs as fine-grained patches that occur with altered feldspar. Anhedral to euhedral, fine-grained magnetite (1%) are disseminated throughout the sample and as an alteration product within amphibole. Zircon (trace) occurs as euhedral, ~50 to 100 μm long inclusions in amphibole and clinopyroxene. Trace, disseminated, fine-grained chalcopyrite occurs as inclusions in magnetite.

The sample was analyzed by single stream LA-ICP-MS. After analysis and data filtering, the resulting weighted mean ^{206}Pb/^{238}U age is 206.8±0.9 Ma (n=12/13; MSWD=1.7; pof=0.06). This crystallization age was further refined from, but within uncertainty of, a previously reported age of sample 19GJ12-4 (206.6±0.9 Ma) by Ootes et al. (2020c) and Jones et al. (2021).

Table 6. Split stream laser ablation-inductively coupled plasma-mass spectrometry (LASS-ICP-MS) parameters for titanite and apatite U-Pb and Sm-Nd analyses.

Laboratory and sample preparation					
Laboratory name	Arctic Resource Lab, University of Alberta (Canada)				
Sample type/mineral	Apatite and titanite grains (magmatic)				
Sample preparation	Conventional mineral separation, polished 1 inch resin mount				
Imaging	CL & BSE (Zeiss EVO LS15) 25kv				
Laser ablation system					
Make, Model & type	RESOlution ArF excimer				
Ablation cell	Laurin Technic S-155				
Laser wavelength	193 nm				
Pulse width	20 ns				
Fluence	ca. 5-6 J.cm^{-2} (120 mJ, 44% transmission)				
Repetition rate	8 Hz				
Ablation/Washout duration	60 secs / 60 secs				
Ablation rate	0.19μm.pulse^{-1}				
Spot diameter	90 μm				
Sampling mode / pattern	Static spot ablation				
Carrier gas and gas flow	A mixture of ~0.85 L/min Ar and 6- 7 ml/min N$_2$, which entered tangentially from the top of the S-155 ablation cell funnel and ~400 ml/min He entering from the side of the cell.				
LA-ICP-MS					
U–Th–Pb measurements					
Make, Model & type	Thermo Fisher Scientific, Element XR, SC-SF-ICP-MS				
Sample introduction	Ablation aerosol introduced through Tygon tubing				
RF power	1360W				
Detection system	202, 208, 232 in triple mode. 206 and 238 in analogue mode. 204 and 207 in counting mode 235 is calculated using canonical value. No Faraday cup used.				
Masses measured	202, 204, 206, 207, 208, 232, 238				
Integration time per peak/ dwell times	30 ms on 202, 204, 208 and 232; 60 ms on 206, 207 and 238				
Total integration time	300 ms for each output datapoint				
IC Dead time	20 ns				
Sm-Nd measurements					
Make, Model & type	Thermo Fisher Scientific, Neptune Plus, MC-SF-ICP-MS				
Sample introduction	Ablation aerosol introduced tygon tubing. Ni-Jet Sample cone and X-Skimmer cone.				
RF power	1250W				
Detection system	Static Faraday (attached to 10^{11} Ω amplifier) measurement				
Masses measured	143, 144, 145, 148, 150				
Cup configuration	L2	L1	Axial	H1	H2
	143	144	145	148	150
Data Processing					
Gas blank	30 second on-peak zero subtracted both for U-Pb and Sm-Nd measurements				
Calibration strategy	Bear Lake titanite and Bancroft apatite used as primary reference material (Sm-Nd), MKED titanite and MAD apatite used as secondaries/validation materials. MKED titanite and MAD apatite used as primary reference material (U-Pb), Bear Lake titanite and Bancroft apatite used as secondaries/validation materials.				
Reference Material info	Bear Lake titanite (Aleinikoff et al., 2007) Bancroft apatite (Fisher et al., 2020) MKED titanite (Spandler et al., 2016) MAD apatite (Fisher et al., 2020)				
Data processing package used / Correction for LIEF	Iolite software package (Paton et al., 2010; Paton et al., 2011; Fisher et al., 2017) using the following DRS: "X_U_Pb Geochron" for U–Th–Pb isotope analyses and "SmNd_Downhole" for Sm-Nd analyses. LIEF correction assumes matrix match between reference material and samples.				
Uncertainty level & propagation	Ages are quoted at a coverage factor of 2, absolute. Propagation is by quadratic addition.				

4.2.4. Thane Creek quartz monzodiorite: 19GJ13-3 (revision of result in Ootes et al. (2020c)

Quartz monzodiorite sample 19GJ13-3 of the Thane Creek suite is from 25.9 km southeast of Notch Peak (Fig. 2). It is a "salt and pepper", fine- to medium-grained, equigranular quartz monzodiorite, composed of 40% euhedral plagioclase, 30% poikilitic alkali feldspar, and 15% anhedral, strained quartz. Mafic minerals make up 10% of the sample, mainly subhedral amphibole (8%) with lesser biotite (2%). Anhedral magnetite and titanite, and euhedral apatite and zircon are accessory. Titanite occurs as 1 mm wide poikilitic grains and as fine rims on magnetite.

The sample was analyzed by single stream LA-ICP-MS. After analysis and data filtering, an excessive scatter constant of 3.25 was applied to the standard error of single data points to lower the MSWD of the weighted mean ^{206}Pb/^{238}U date. The resulting weighted mean ^{206}Pb/^{238}U date is 194.0±1.0 Ma (n=38/50; MSWD=1.3; pof=0.11). This crystallization age was further refined from, but within uncertainty of, a previously reported age of sample 19GJ13-3 (194.0±1.1 Ma) by Ootes et al. (2020c) and Jones et al. (2021).

4.2.5. Duckling Creek syenite: 18lo25-2a (revision of result in Ootes et al. (2020c)

Syenite sample 18lo25-2a of the Duckling Creek suite is from 22.7 km southeast of Notch Peak (Fig. 2). The rock is a pink-white, medium-grained, equigranular syenite. The sample consists of 90% two alkali feldspars (K- and Na-bearing), with lesser clinopyroxene (5%). Magnetite (2%), titanite (1%), chlorite (1%), and zircon (<1%) are accessory minerals. Titanite occurs as 1 mm wide euhedral, wedge-shaped grains with clinopyroxene.

Two types of zircons were identified during mineral picking. 'Type one' zircons (Appendix 2; zircon images labelled 18lo25-2a z1) are clear-pink coloured fragments between 100 and 200 µm long. 'Type two' zircons (Appendix 2; zircon images labelled 18lo25-2a z2) are larger grains (300 to 400 µm) that are brown with good crystal habit. The cores of these zircons are commonly metamict or highly fractured. The results of U-Pb for both zircon types are included together.

The sample was analyzed by split stream LA-ICP-MS. After data filtering, an excessive scatter contact of 1.63 was applied to the standard error of single data points to lower the MSWD of the weighted mean ^{206}Pb/^{238}U date. The resulting weighted mean ^{206}Pb/^{238}U age is 179.0±1.0 Ma (n=20/44; MSWD=1.0; pof=0.46). This crystallization age was further refined from, but within uncertainty of, a previously reported age of sample 18lo25-2a (178.9±1.3 Ma) by Ootes et al. (2020c) and Jones et al. (2021).

4.2.6. Duckling Creek syenite: 19GJ13-5a (previously reported in Ootes et al. (2020c)

Syenite sample 19GJ13-5a of the Duckling Creek suite is from 31.1 km southwest of Notch Peak (Fig. 2). The sample was collected next to the Slide Cu-Au porphyry prospect, and 7 m south of a grab sample with chalcopyrite that yielded 0.07 wt.% Cu (19GJ13-5b; Ootes et al., 2020b). It is a pink-white and greenish-black, medium-grained, equigranular syenite. It contains alkali feldspar (~70%), with lesser amphibole (9%), plagioclase (8%), and clinopyroxene (5%). Biotite, chlorite, and magnetite combine to make up ~5% of the sample, while fine-grained apatite, titanite, epidote, and zircon are trace (<1%) accessory minerals. Chalcopyrite occurs as rare fine, disseminated grains, and may be rimmed by titanite.

The sample was analyzed by single stream LA-ICP-MS. After analysis and data filtering, the resulting weighted mean ^{206}Pb/^{238}U age is 174.7±0.7 Ma (n=24/26; MSWD=1.4; pof=0.12).

4.2.7. Osilinka granite: 18lo17-1 (previously reported in Ootes et al. (2020c)

Granite sample 18lo17-1 of the Osilinka suite is from 11.9 km southeast of Notch Peak (Fig. 2). The rock is a white (leucocratic), medium-grained, equigranular granite. Strained quartz (~37%), subhedral alkali feldspar (32%), and subhedral plagioclase (26%) comprise most of the sample. Rare accessory biotite, muscovite, and magnetite constitute less than 5% of the rock. Fine-grained biotite and magnetite occur interstitial to feldspar grains, whereas muscovite and sericite are present within feldspar cores and along grain boundaries. Trace euhedral zircon grains are found as inclusions within quartz.

The sample was analyzed by split stream LA-ICP-MS. The thirteen remaining zircon grains after filtering are interpreted as inherited, and the youngest zircon has a ^{206}Pb/^{238}U date of 159.2±4 Ma, which is interpreted as the maximum age for crystallization.

4.2.8. Osilinka porphyry sheet: 18lo20-4 (previously reported in Ootes et al. (2020c)

Porphyry sheet sample 18lo20-4 is from a flat-lying dike that cuts the Osilinka suite, 14.0 km southeast of Notch Peak (Fig. 2). The dike is at least 4 m thick. Fine-grained plagioclase and quartz make up most of the groundmass, with plagioclase phenocrysts up to 0.5 cm. Magnetite, chlorite, epidote, and calcite are accessory groundmass minerals. Rare ~2.5 mm wide euhedral chalcopyrite grains also occur in the groundmass. A ~0.5 mm wide calcite-filled vein cuts the sample.

The sample was analyzed by split stream LA-ICP-MS. After filtering, nine remaining analyses are interpreted as xenocrysts, and the youngest zircon has a ^{206}Pb/^{238}U date of 162.2±2.6 Ma, which is interpreted as the maximum age for crystallization.

4.2.9. Osilinka granite: 19GJ12-3 (new age)

Granite sample 19GJ12-3 of the Osilinka suite is from 6.1 km east of Notch Peak (Fig. 2). The rock is a white (leucocratic), medium-grained, equigranular granite. Strained quartz (~30%), subhedral alkali feldspar (29%), and subhedral plagioclase (35%) comprise most of the sample. Muscovite/sericite (5%), biotite (1%), epidote (trace), magnetite (trace), pyrite (trace), and zircon (trace) are accessory minerals. Muscovite/sericite is fine-grained, anhedral and occurs as an alteration product of feldspar. Biotite and magnetite are spatially associated, very fine-grained, and disseminated. Epidote is fine-grained, anhedral, fractured, and disseminated through the sample. Rare, anhedral pyrite occurs as fine, disseminated grains rimmed by hematite. Rare, euhedral ~100 µm long zircon grains are found as inclusions in feldspar and quartz.

After analysis and data filtering, six remaining zircons yield a 42.6 million year spread in ^{206}Pb/^{238}U dates and are interpreted as inherited. The youngest zircon has a ^{206}Pb/^{238}U date of 187.7±3.8 Ma. This zircon grain is also interpreted as inherited, due to the presence of younger (ca. 160 Ma) zircons in Osilinka granite 18lo17-1 and porphyry sheet 18lo20-4. Additionally, field relationships indicate the Osilinka granite cross-cuts Duckling Creek syenites (ca. 179 to 174 Ma), thus the Osilinka granite must be younger than at least ca. 174 Ma.

4.2.10. Mesilinka equigranular granite: 18lo11-1 (revision of result in Ootes et al. (2020c)

Equigranular granite sample 18lo11-1 of the Mesilinka suite is from 1.5 km northeast of Horn Peak (Fig. 2). The rock is an equigranular, fine to medium-grained granite with a foliation defined by biotite. The sample is mostly strained fine-grained quartz (40%), anhedral medium-grained alkali feldspar (30%), and clay-altered plagioclase (25%). Accessory minerals include zircon, fine-grained muscovite, biotite, and magnetite. Magnetite may be rimmed by titanite.

The sample was analyzed by split stream LA-ICP-MS. After data filtering, an excessive scatter constant of 2.23 was applied to the standard error of single data points to lower the MSWD of the weighted mean ^{206}Pb/^{238}U date. The resulting weighted mean ^{206}Pb/^{238}U age is 127.7±0.8 Ma (n=34/48; MSWD=1.5; pof=0.02). This crystallization age was further refined from, but within uncertainty of, a previously reported age of sample 18lo11-1 (127.9±0.8 Ma) by Ootes et al. (2020c) and Jones et al. (2021).

4.2.11. Mesilinka K-feldspar porphyritic granite: 18lo12-7 (revision of result in Ootes et al. (2020c)

K-feldspar porphyritic granite sample 18lo12-7 of the Mesilinka suite is from 2.1 km northeast of Horn Peak (Fig. 2). The rock is a medium-grained K-feldspar porphyritic granite with a foliation defined by biotite. Clay-altered alkali feldspar phenocrysts up to 5 cm (38%), strained anhedral quartz (28%), and myrmekitic plagioclase (22%) comprise most of the sample. Biotite (10%) is 1 to 2 mm wide and interstitial to feldspar and quartz. Accessory minerals include zircon, magnetite, apatite, epidote, and allanite with epidote rims.

The sample was analyzed by split stream LA-ICP-MS. After data filtering, an excessive scatter constant of 2.18 was applied to the standard error of single data points to lower the MSWD of the weighted mean ^{206}Pb/^{238}U date. The resulting weighted mean ^{206}Pb/^{238}U age is 135.4±0.9 Ma (n=20/33; MSWD=1.4; pof=0.11). This crystallization age was further refined from, but within uncertainty of, a previously reported age of sample 18lo12-7 (134.8±1.2 Ma) by Ootes et al. (2020c) and Jones et al. (2021).

4.2.12. Mesilinka tonalite: 19GJ12-1 (previously reported in Ootes et al. (2020c)

Tonalite sample 19GJ12-1 of the Mesilinka suite is from 2.4 km northwest of Horn Peak (Fig. 2). The rock is a grey, medium-grained, equigranular biotite-rich tonalite with a foliation defined by biotite. Equigranular granite dikes cut the tonalite in outcrop ~50 m away. The sample is composed of slightly clay-altered, subhedral plagioclase (~50%), with lesser anhedral, strained quartz (~30%) and brown and green biotite (~15%). Subhedral amphibole (2%) and magnetite (trace) are spatially associated with biotite. Trace fine-grained anhedral epidote and titanite, and euhedral apatite and zircon occur with and as inclusions in biotite.

The sample was analyzed by single stream LA-ICP-MS. After data filtering, the resulting weighted mean ^{206}Pb/^{238}U date is 134.1 ± 0.5 Ma (n=18/23; MSWD=1.5; pof=0.09), which we interpret records the time of crystallization.

4.2.13. Mesilinka equigranular granite: 19GJ16-2 (new age)

Equigranular granite sample 19GJ16-2 of the Mesilinka suite is from 11.8 km southeast of Mount Ferris (Fig. 2). The rock is a pinkish-white and black, fine to medium-grained, equigranular granite. The sample is composed of slightly altered, anhedral K-feldspar (~40%), with subhedral, variably myrmekitic plagioclase (~32%), and anhedral, strained quartz (~22%). Minor anhedral, fine-grained brown biotite (2%) occurs interstitially to the main minerals and is variably altered to chlorite (1%). Apatite, epidote, magnetite, titanite, allanite, muscovite, zircon, chalcopyrite, and bornite are accessory. Apatite (1%) occurs as very fine-grained, euhedral inclusions within biotite. Subhedral, very fine magnetite (1%), fine anhedral epidote (trace), and fine anhedral titanite (trace) grains are spatially associated with biotite. Rare, euhedral, fine-grained zoned allanite (trace) are rimmed by epidote. Euhedral, ~50 to 60 µm long zircon (trace) grains are inclusions in biotite, quartz, and feldspar. Chalcopyrite and bornite are rare, very fine-grained inclusions in magnetite.

The sample was analyzed by single stream LA-ICP-MS. After data filtering, an excessive scatter constant of 2.58 was applied to the standard error of single data points to lower the MSWD of the weighted mean ^{206}Pb/^{238}U date. The resulting weighted mean ^{206}Pb/^{238}U age is 127.1±1.6 Ma (n=13/33; MSWD=1.4; pof=0.18) and is interpreted as the crystallization age for sample 19GJ16-2.

4.3. LASS-ICP-MS titanite U-Pb results

Supporting data for titanite LASS-ICP-MS U-Pb results are in Appendix 9. Titanite LA-ICP-MS U-Pb results are plotted on Tera-Wasserburg diagrams using uncorrected ^{238}U/^{206}Pb and ^{207}Pb/^{206}Pb ratios. Titanite crystallization ages were calculated using a regression approach, in which an isochron fit through the data defines a mixing line between the common Pb composition (upper intercept) and the radiogenic U-Pb cooling age (lower intercept) of the titanite population for each sample. Individual data points that did not overlap with the regression line were excluded to reduce scatter, indicated by MSWD and p(χ^2) values closer to one.

4.3.1. Thane Creek quartz monzodiorite: 19GJ13-3 (new age)

A description of the Thane Creek Quartz monzodiorite sample 19GJ13-3 is in section 4.2.4. Titanite grains from the sample have a U-Pb intercept age of 197.5±3.7 Ma. Five titanite results were excluded from the regression to reduce scatter, yielding an MSWD of 2.4 (n=9/14). This titanite U-Pb intercept age overlaps with the interpreted zircon LA-ICP-MS U-Pb crystallization age of the same sample (194.0±1.1 Ma; section 4.2.4). The titanite U-Pb intercept age is interpreted as the magmatic crystallization age of titanite, which occurred before and during zircon crystallization. Petrographic identification of zircon inclusions within titanite grains in sample 19GJ13-3 supports this interpretation.

4.3.2. Duckling Creek syenite: 19GJ13-2 (new age)

Syenite sample 19GJ13-2 of the Duckling Creek suite is from 18.2 km southeast of Notch Peak (Fig. 2). It is a pink-white and greenish-black, coarse-grained, K-feldspar phenocrystic syenite. The rock comprises predominantly >2cm long alkali feldspar phenocrysts (~85%). Muscovite (10%), epidote (2%), magnetite (1%), biotite (1%), and quartz (trace) occur as fine-grained intergrown patches interstitial to K-feldspar phenocrysts. Subhedral fine-grained titanite (trace) occurs with magnetite. Rare, disseminated, fine-grained chalcopyrite grains are spatially associated with biotite inclusions within K-feldspar.

Titanite grains from Duckling Creek syenite sample 19GJ13-2 have a U-Pb intercept age of 177.4±7.0 Ma. One titanite result was excluded from the regression to reduce scatter, yielding an MSWD of 1.9 and p(χ^2) of 0.09 (n=7/8). This titanite U-Pb intercept age may be interpreted as the magmatic crystallization age of titanite, due to the overlap with interpreted U-Pb zircon crystallization ages of two other Duckling Creek syenite samples (179.0±1.0 Ma and 174.7±0.7 Ma; section 4.2.5 and 4.2.6). It is unclear if titanite grains in sample 19GJ13-2 are magmatic because subhedral titanite grains are spatially associated with biotite inclusions in feldspar, and form intercumulus patches with magmatic biotite, magnetite, and secondary muscovite and epidote between K-feldspar phenocrysts.

4.3.3. Duckling Creek syenite: 19GJ13-4 (new age)

Duckling Creek suite syenite sample 19GJ13-4 is from 28.9 km southeast of Notch Peak (Fig. 2). It is a pink and greenish-black, medium-grained, foliated syenite. The sample consists of ~80% anhedral, clay-altered alkali feldspar with lesser anhedral clinopyroxene (~8%) and amphibole (~5%). Biotite (2%) occurs as fine grains along clinopyroxene grain boundaries, has magnetite inclusions within cleavage, and is spatially associated with chlorite (2%). Magnetite (1%), muscovite (1%), apatite (1%), epidote (trace), and titanite (trace) are accessory minerals. Subhedral magnetite is generally very fine grained and disseminated throughout the sample and concentrated with other mafic minerals. Muscovite is very fine grained and occurs with epidote, biotite, and chlorite. Fine-grained euhedral apatite and anhedral titanite are spatially associated and occur interstitially to K-feldspar.

Titanite grains from Duckling Creek syenite sample 19GJ13-4 have a U-Pb intercept age of 174.4±2.2 Ma. One titanite result was excluded from the regression to reduce scatter, yielding an MSWD of 1.7 and probability of fit of 0.13 (n=7/8). This titanite U-Pb intercept age is interpreted as the magmatic crystallization age of titanite, due to the overlap and close agreement with the interpreted zircon U-Pb crystallization age of Duckling Creek syenite sample 19GJ13-5a (174.7±0.7 Ma; section 4.2.6). Titanite grains in sample 19GJ13-4 appear magmatic in thin section, because they form subhedral to euhedral, wedge-shaped crystals spatially associated with amphibole, biotite, and apatite.

4.3.4. Mesilinka tonalite: 19GJ12-2 (new age)

Tonalite sample 19GJ12-2 of the Mesilinka suite is from 2.5 km northeast of Horn Peak (Fig. 2). It is a grey, fine-grained, equigranular biotite-rich tonalite. The sample is composed of slightly clay-altered, subhedral plagioclase (~48%), with myrmekitic quartz (~33%), and euhedral, bimodal (very fine- and fine-grained) biotite (~16%). Minor subhedral, fine-grained amphibole (2%) occurs with biotite and epidote. Apatite, epidote, magnetite, and titanite are accessory. Apatite (trace) occurs as very fine-grained, euhedral inclusions within feldspar, quartz, and biotite. Fine, anhedral epidote (1%) grains are spatially associated with biotite and may have rare allanite cores. Trace, fine-grained subhedral magnetite (trace) and anhedral titanite occur with biotite.

Titanite grains from Mesilinka tonalite sample 19GJ12-2 have a U-Pb intercept age of 145.8±4.6 Ma. Two titanite data points were excluded from the regression to reduce scatter, yielding an MSWD of 1.5 and probability of fit of 0.17 (n=7/9). This titanite U-Pb intercept age is interpreted as the magmatic crystallization age of titanite. Sample 19GJ12-2 failed to yield zircons, thus the titanite age is the best current estimate for crystallization of this unit.

4.3.5. Mesilinka tonalite: 19GJ12-1

The description for Mesilinka tonalite sample 19GJ12-1 is in section 4.2.12. Titanite grains from Mesilinka tonalite sample 19GJ12-1 have a U-Pb intercept age of 122.0±2.8 Ma. Five titanite data points were excluded from the regression to reduce scatter, yielding an MSWD of 2.8 (n=7/12), which indicates scatter in the data. Titanite grains in sample 19GJ12-1 are spatially associated with biotite, epidote, and apatite, and define a weak foliation. Because the titanite U-Pb intercept age is younger than the interpreted zircon crystallization age of sample 19GJ12-1 (134.1±0.5 Ma; section 4.2.12), we interpret that this titanite U-Pb intercept age records crystallization during cooling of the Mesilinka suite. However, the scatter in the data (MSWD >2) and exclusion of multiple results makes this interpretation tentative.

4.4. LA- and LASS-ICP-MS zircon Lu-Hf isotope results

Zircon LA- and LASS-ICP-MS Lu-Hf isotope results are in Appendices 5, 7, and 8. Overall, Hogem batholith zircons record relatively juvenile, suprachondritic ($\varepsilon Hf_{(t)}$ >0) Lu-Hf isotope compositions. Zircons from the oldest Thane Creek intrusive suite have the most juvenile (mantle-like) $\varepsilon Hf_{(t)}$ values, ranging from +8.2±1.6 to +12.1±1.5. Duckling Creek intrusive suite zircon grains record $\varepsilon Hf_{(t)}$ values of +7.8±1.9 to +10.6±1.4. Zircon grains from Osilinka suite have the widest range in $\varepsilon Hf_{(t)}$ values, from -10.2±1.0 to +10.2±1.5. However, the less radiogenic (i.e., more evolved) εHf(t) values (<+5.0ε) are restricted to porphyry sheet sample 18lo20-4. Zircon grains from Mesilinka suite have the least radiogenic $\varepsilon Hf_{(t)}$ values on average but are overall relatively juvenile (εHf(t) >+4), ranging from +4.8±1.0 to +12.5±1.8.

4.5. LA- and LASS-ICP-MS zircon trace element results

Zircon LA- and LASS-ICP-MS trace element results are in Appendices 6 and 8. Zircons from Hogem batholith have typical chondrite-normalized rare earth element trends, with enriched heavy rare earth elements (REEs) relative to light REEs, positive Ce-anomalies, and negative Eu-anomalies. Duckling Creek syenite sample 18lo25-2a is an exception, as zircons from this sample have positive Ce-anomalies but lack Eu-anomalies (Appendix 6).

4.6. LASS-ICP-MS apatite and titanite Sm-Nd isotope results

Apatite and titanite LASS-ICP-MS Sm-Nd results are in Appendix 9. Overall, the apatite and titanite Sm-Nd results record similar juvenile compositions to zircon Lu-Hf results from the same intrusive suites. Apatite and titanite grains from Thane Creek intrusive suite samples range in $\varepsilon Nd_{(t)}$ from +1.5±1.8 to +5.9±1.7, which convert to $\varepsilon Hf_{(t)}$ values from +5.5 to +10.3. Titanite grains from Duckling Creek intrusive suite samples have $\varepsilon Nd_{(t)}$ values from +2.6±1.2 to +5.6±1.7 and correspond to $\varepsilon Hf_{(t)}$ ranging from +5.3 to +10.9. Titanite grains from Mesilinka intrusive suite samples range in $\varepsilon Nd_{(t)}$ from +1.9±1.8 to +5.1±1.6 and convert to $\varepsilon Hf_{(t)}$ values from +4.1 to +9.2.

5. Conclusion

New and refined mineral geochronology and geochemistry data from northern Hogem batholith reveal that four predominantly juvenile ($\varepsilon Hf_{(t)}$ >0) intrusive suites were emplaced during a prolonged period (ca. 80 Ma), between 207 and 128 Ma.

Acknowledgements

The first author acknowledges support from the Diamond Exploration Research Training School (DERTS), which is funded by NSERC and the University of Alberta. The first author received additional funding from NSERC CGS-M and Geoscience BC. We are grateful for field assistance from A. Bergen, B. Graham, R. Simmonds, D. Spence, S. Rauhala, K. Shortridge, M. Farhat, and J. Lockie.

References cited

Aleinikoff, J.N., Wintsch, R.P., Tollo, R.P., Unruh, D.M., Fanning, C.M., and Schmitz, M.D., 2007. Ages and origins of rocks of the Killingworth dome, south-central Connecticut: implications for the tectonic evolution of southern New England. American Journal of Science, 307, 63-119. https://doi.org/10.2475/01.2007.04

Baertschi, P., 1976. Absolute ^{18}O content of standard mean ocean water. Earth and Planetary Science Letters, 31, 341-344. https://doi.org/10.1016/0012-821X(76)90115-1

Black, L.P., Kamo, S.L., Allen, C.M., Davis, D.W., Aleinikoff, J.N., Valley, J.W., Mundil, R., Campbell. I.H., Korsch, R.J., Williams, I.S., and Foudoulis, C., 2004. Improved ^{206}Pb/^{238}U microprobe geochronology by the monitoring of a trace-element-related matrix effect; SHRIMP, ID-TIMS, ELA-ICP-MS and oxygen isotope documentation for a series of zircon standards. Chemical Geology, 205, 115-140. https://doi.org/10.1016/j.chemgeo.2004.01.003

Blichert-Toft, J., 2008. The Hf isotopic composition of zircon reference material 91500. Chemical Geology, 253, 252-257. https://doi.org/10.1016/j.chemgeo.2008.05.014

Bouvier, A., Vervoort, J.D., and Patchett, P.J., 2008. The Lu–Hf and Sm–Nd isotopic composition of CHUR: Constraints from unequilibrated chondrites and implications for the bulk composition of terrestrial planets. Earth and Planetary Science Letters, 273, 48-57. https://doi.org/10.1016/j.epsl.2008.06.010

Colpron, M. and Nelson, J.L., 2020. A digital atlas of terranes for the northern Cordillera. Yukon Geological Survey. http://data.geology.gov.yk.ca/Compilation/2

Currie, L.A., 1968. Limits for qualitative detection and quantitative determination. Application to radiochemistry. Analytical Chemistry, 40, 586–593. https://doi.org/10.1021/ac60259a007

Devine, F.A.M., Chamberlain, C.M., Davies, A.G.S., Friedman, R., and Baxter, P., 2014. Geology and district-scale setting of tilted alkalic porphyry Cu-Au mineralization at the Lorraine deposit, British Columbia. Economic Geology, 109, 939-977. https://doi.org/10.2113/econgeo.109.4.939

Fisher, C.M., Hanchar, J.M., Samson, S.D., Dhuime, B., Blichert-Toft, J., Vervoort, J.D., and Lam, R., 2011. Synthetic zircon doped with hafnium and rare earth elements: A reference material for in situ hafnium isotope analysis. Chemical Geology, 286, 32-47. https://doi.org/10.1016/j.chemgeo.2011.04.013

Fisher, C.M., Vervoort, J.D., and DuFrane, S.A., 2014. Accurate Hf isotope determinations of complex zircons using the "laser ablation split stream" method. Geochemistry, Geophysics, Geosystems, 15, 121-139. https://doi.org/10.1002/2013GC004962

Fisher, C.M., Bauer, A.M., Luo, Y., Sarkar, C., Hanchar, J.M., Vervoort, J.D., Tapster, S.R., Horstwood, M., and Pearson, D.G., 2020. Laser ablation split-stream analysis of the Sm-Nd and U-Pb isotope compositions of monazite, titanite, and apatite – Improvements, potential reference materials, and application to the Archean Saglek Block gneisses. Chemical Geology, 539, 119493. https://doi.org/10.1016/j.chemgeo.2020.119493

Gain, S.E.M, Greau, Y., Henry, H., Belousova, E., Dainis, I., Griffin, W.L., and O'Reilly, S.Y., 2019. Mud Tank zircon: Long term evaluation of a reference material for U-Pb dating, Hf-isotope analysis and trace element analysis. Geostandards and Geoanalytical Research, 43 339-345. https://doi.org/10.1111/ggr.12265

Ickert, R.B., 2013. Algorithms for estimating uncertainties in initial radiogenic isotope ratios and model ages. Chemical Geology, 340, 131-138. https://doi.org/10.1016/j.chemgeo.2013.01.001

Jaffey, A.H., Flynn, K.F., Glendenin, L.E., Bentley, W.C., and Essling, A.M., 1971. Precision measurements of half-lives and specific activities of ^{235}U and ^{238}U. Physical Reviews, C4, 1889-1906. https://doi.org/10.1103/PhysRevC.4.1889

Jones, G., 2022. Implications of in situ zircon U-Pb, Lu-Hf, oxygen-isotope, and trace element geochemistry on the petrogenetic history of the northern Hogem batholith in the Quesnel terrane, north-central British Columbia, Canadian Cordillera. Unpublished M.Sc. thesis, University of Alberta, Edmonton, Canada, 396p.

Jones, G., Ootes, L., Milidragovic, D., Friedman, R., Camacho, A., Luo, Y., Vezinet, A., Pearson, D.G., and Schiarizza, P., 2021. Geochronology of northern Hogem batholith, Quesnel terrane, north-central British Columbia. In: Geological Fieldwork 2020, British Columbia Ministry of Energy, Mines and Low Carbon Innovation, British Columbia Geological Survey Paper 2021-01, pp. 37-56.

Klepeis, K.A., Crawford, M.L., and Gehrels, G., 1998. Structural history of the crustal-scale Coast shear zone north of Portland Canal, southeast Alaska and British Columbia. Journal of Structural Geology, 20, 883-904. https://doi.org/10.1016/S0191-8141(98)00020-0

Longerich, H.P., Jackson, S.E., and Günther, D., 1996. Laser ablation inductively coupled plasma mass spectrometric transient signal data acquisition and analyte concentration calculation. Journal of Analytical Atomic Spectrometry, 11, 899-904. https://doi.org/10.1039/JA9961100899

Loucks, R.R., Fiorentini, M.L., and Henríquez, G.J., 2020. New magmatic oxybarometer using trace elements in zircon. Journal of Petrology, 61, 1-30. https://doi.org/10.1093/petrology/egaa034

Lugmair, G.W., and Marti, K., 1978. Lunar initial ^{143}Nd/^{144}Nd: differential evolution of the lunar crust and mantle. Earth and Planetary Science Letters, 39, 349-357. https://doi.org/10.1016/0012-821X(78)90021-3

Ootes, L., Bergen, A.L., Milidragovic, D., Graham, B., and Simmonds, R., 2019. Preliminary geology of northern Hogem batholith, Quesnel terrane, north-central British Columbia. In: Geological Fieldwork 2018, British Columbia Ministry of Energy, Mines and Petroleum Resources, British Columbia Geological Survey Paper 2019-01, pp. 31-53.

Ootes, L., Bergen, A.L., Milidragovic, D., and Jones, G.O., 2020a. Bedrock geology of the northern Hogem batholith and its surroundings, north-central British Columbia. British Columbia Ministry of Energy and Mines and Petroleum Resources, British Columbia Geological Survey Open File 2020-02, scale 1:50,000.

Ootes, L., Bergen, A.L., Milidragovic, D., Jones, G.O., Camacho, A., and Friedman, R., 2020b. An update on the geology of northern Hogem batholith and its surroundings, north-central British Columbia. In: Geological Fieldwork 2019, British Columbia Ministry of Energy, Mines and Petroleum Resources, British Columbia Geological Survey Paper 2020-01, pp. 25-47.

Ootes, L., Jones, G., Schiarizza, P., Milidragovic, D., Friedman, R., Camacho, A., Luo, Y., Vezinet, A., Pearson, D.G., and Zhang, S., 2020c. Geochronologic and geochemical data from northern Hogem batholith and its surroundings, north-central British Columbia. British Columbia Ministry of Energy, Mines and Low Carbon Innovation, British Columbia Geological Survey GeoFile 2020-01, 21p.

Paton, C., Woodhead, J.D., Hellstrom, J.C., Hergt, J.M., Greig, A., and Maas, R., 2010. Improved laser ablation U-Pb zircon geochronology through robust downhole fractionation correction. Geochemistry, Geophysics, Geosystems, 11. https://doi.org/10.1029/2009GC002618

Paton, C., Hellstrom, J., Paul, B., Woodhead, J., and Hergt, J., 2011. Iolite: Freeware for the visualization and processing of mass spectrometric data. Journal of Analytical Atomic Spectrometry, 26, 2508-2518. https://doi.org/10.1039/C1JA10172B

Pettke, T., Oberli, F., Audetat, A., Guillong, M., Simon, A.C., Hanley, J.J., and Klemm, L.M., 2012. Recent developments in element concentration and isotope ratio analysis of individual fluid inclusions by laser ablation single and multiple collector ICP-MS. Ore Geology Reviews, 44,10-38. https://doi.org/10.1016/j.oregeorev.2011.11.001

Rosman, K.J.R., and Taylor, P.D.P., 1998. Isotopic compositions of the elements 1997 (Technical Report). Pure and Applied Chemistry, 71, 217-235. https://doi.org/10.1351/pac199870010217

Russell, W., Papanastassiou, D., and Tombrello, T., 1978. Ca isotope fractionation on the Earth and other solar system materials. Geochimica et Cosmochimica Acta, 42, 1075-1090. https://doi.org/10.1016/0016-7037(78)90105-9

Schiarizza, P., and Tan, S.H., 2005a. Geology and mineral occurrences of the Quesnel Terrane between the Mesilinka River and Wrede Creek (NTS 94D/8, 9), north-central British Columbia. British Columbia Ministry of Energy and Mines, British Columbia Geological Survey Paper 2005-1, pp. 109-130.

Schiarizza, P., and Tan, S.H., 2005b. Geology of the Johanson Lake area, parts of NTS 94D/8 and 9. British Columbia Ministry of Energy, Mines and Petroleum Resources, British Columbia Geological Survey Open File 2005-4, scale 1:50,000.

Sláma, J., Košler, J, Condon, D.J., Crowley, J.L., Gerdes, A., Hanchar, J.M., Horstwood, M.S.A., Morris, G.A., Nasdala, L., Norberg, N., Schaltegger, U., Schoene, B., Tubrett, M.N., and Whitehouse, M.J., 2008. Plešovice zircon – A new natural reference material for U–Pb and Hf isotopic microanalysis. Chemical Geology, 249, 1-35. https://doi.org/10.1016/j.chemgeo.2007.11.005

Söderlund, U., Patchett, P.J., Vervoort, J.D. and Isachsen, C.E., 2004. The ^{176}Lu decay constant determined by Lu-Hf and U-Pb isotope systematics of Precambrian mafic intrusions. Earth and Planetary Science Letters, 219, 311-324. https://doi.org/10.1016/S0012-821X(04)00012-3

Spandler, C., Hammerli, J., Sha, P., Hilbert-Wolf, H., Hu, Y., Roberts, E., and Schmitz, M., 2016. MKED1: A new titanite standard for in situ analysis of Sm–Nd isotopes and U–Pb geochronology. Chemical Geology, 425, 110-126. https://doi.org/10.1016/j.chemgeo.2016.01.002

Stacey, J.S., and Kramers, J.D., 1975. Approximation of terrestrial lead isotope evolution by a two-stage model. Earth and Planetary Science Letters, 26, 207-221. https://doi.org/10.1016/0012-821X(75)90088-6

Sun, S.S., and McDonough, W.F., 1989. Chemical and isotopic systematics of oceanic basalts; implications for mantle composition and processes. In: Saunders, A.D. and Norry, M.J. (Eds.), Magmatism in the Ocean Basins. Geological Society of London, Special Publication, 42, pp. 313-345. https://doi.org/10.1144/GSL.SP.1989.042.01.19

Valley, J., Kinny, P., Schulze, D., and Spicuzza, M.J., 1998. Zircon megacrysts from kimberlite: oxygen isotope variability among mantle melts. Contributions to Mineralogy and Petrology, 133, 1-11. https://doi.org/10.1007/s004100050432

Valley, J.W., Lackey, J.S., Cavosie, A.J., Clechenko, C.C., Spicuzza, M.J., Basei, M.A.S., Bindeman, I.N., Ferreira, V.P., Sial, A.N., King, E.M., Peck, W.H., Sinha, A.K., and Wei, C.S., 2005. 4.4 billion years of crustal maturation: oxygen isotope ratios of magmatic zircon. Contributions to Mineralogy and Petrology, 150, 561-580. https://doi.org/10.1007/s00410-005-0025-8

Vermeesch, P., 2018. IsoplotR: A free and open toolbox for geochronology. Geoscience Frontiers, 9, 1479-1493. https://doi.org/10.1016/j.gsf.2018.04.001

Vervoort, J.D., Plank, T., and Prytulak, J., 2011. The Hf-Nd isotopic composition of marine sediments. Geochimica et Cosmochimica Acta, 75, 5903-5926. https://doi.org/10.1016/j.gca.2011.07.046

Vezinet, A., Pearson, D.G., Thomassot, E., Stern, R.A., Sarkar, C., Luo, Y., and Fisher, C.M., 2018. Hydrothermally-altered mafic crust as source for early Earth TTG: Pb/Hf/O isotope and trace element evidence from TTG of the Eoarchean Saglek Block, N. Labrador (electronic supplementary material). Earth and Planetary Science Letters, 503, 95-107. https://doi.org/10.1016/j.epsl.2018.09.015

Wiedenbeck, M., Allé, P., Corfu, D., Griffin, W.L., Meier, M., Oberli, F., Von Quadt, A., Roddick, J.C., and Spiegel, W., 1995. Three natural zircon standards for U-Th-Pb, Lu-Hf, trace element and REE Analyses. Geostandards Newsletter, 19, 1-23. https://doi.org/10.1111/j.1751-908X.1995.tb00147.x

Wiedenbeck, M., Hanchar, J.M., Peck, W.H., Sylvester, P., Valley, J., Whitehouse, M., Kronz, A., Morishita, Y., Nasdala, L., Fiebig, J., Franchi, I., Girard, J.-P., Greenwood, R.C., Hinton, R., Kita, N., Mason, P.R.D., Norman, M., Ogasawara, M., Piccoli, P.M., Rhede, D., Satoh, H., Schulz-Dobrick, B., Skår, Ø., Spicuzza, M.J., Terada, K., Tindle, A., Togashi, S., Vennemann, T., Xie, Q., and Zheng, Y.-F., 2004. Further characterisation of the 91500 zircon crystal. Geostandards and Geoanalytical Research, 28, 9-39. https://doi.org/10.1111/j.1751-908X.2004.tb01041.x

Woodhead, J., Hergt, J., Shelley, M., Eggins, S., and Kemp, R., 2004. Zircon Hf-isotope analysis with an excimer laser, depth profiling, ablation of complex geometries, and concomitant age estimation. Chemical Geology, 209, 121-135. https://doi.org/10.1016/j.chemgeo.2004.04.026

Woodsworth, G.J., 1976. Plutonic rocks of McConnell Creek (94 D west half) and Aiken Lake (94 C east half) map-areas, British Columbia. In: Blackadar, R.G., Griffin, P.J., Dumych, H. (Eds.), Report of Activities, Part A. Geological Survey of Canada, Paper 76-1A, pp. 69-73. https://doi.org/10.4095/119844

Zhong, S., Seltmann, R., Qu, H., and Song, Y., 2019. Characterization of the zircon Ce anomaly for estimation of oxidation state of magmas: A revised Ce/Ce* method. Mineralogy and Petrology, 113,755–763. https://doi.org/10.1007/ s00710-019-00682-y

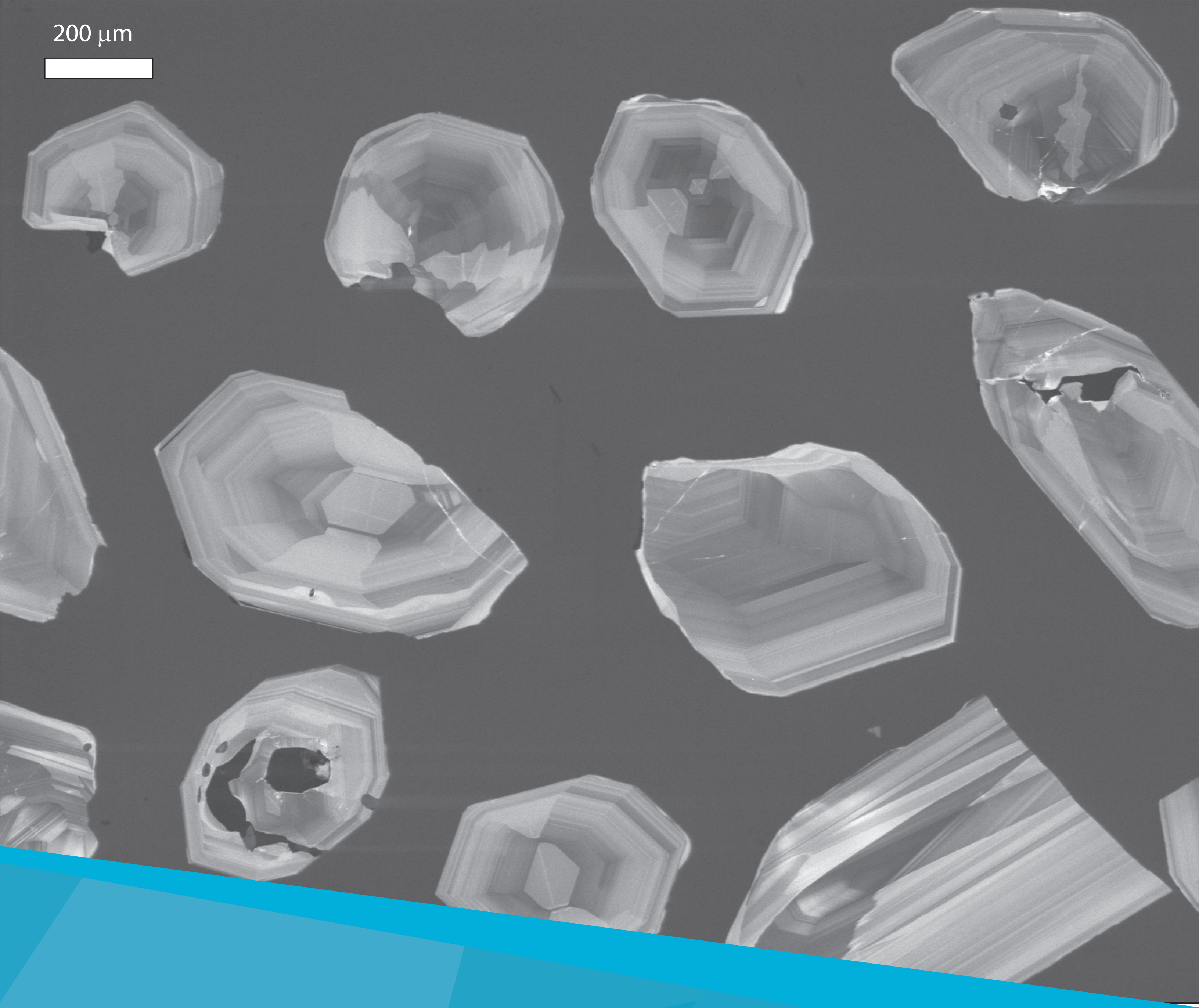

BRITISH
COLUMBIA

Ministry of
Energy, Mines and
Low Carbon Innovation

BRITISH COLUMBIA
est. 1895
GEOLOGICAL SURVEY